Author Manuscript

Author Manuscript

Author Manuscript

Author Manuscript

HHS Public Access

Author manuscript

Cancer Res. Author manuscript; available in PMC 2022 November 16.

Published in final edited form as:

Cancer Res. 2022 May 16; 82(10): 1969–1990. doi:10.1158/0008-5472.CAN-21-3155.

Carbon monoxide activates PERK-regulated autophagy to induce immunometabolic reprogramming and boost anti-tumor T cell function

Paramita Chakraborty[1,#], **Rasesh Y. Parikh**[2], **Seungho Choi**[1], **Danh Tran**[1], **Monika Gooz**[3], **Zachariah T. Hedley**[1], **Do-Sung Kim**[1], **Dariusz Pytel**[2,11], **Inhong Kang**[4], **Satish N. Nadig**[1], **Gyda C. Beeson**[3], **Lauren Ball**[5], **Meenal Mehrotra**[4], **Hongjun Wang**[1], **Stefano Berto**[6], **Viswanathan Palanisamy**[2], **Hong Li**[7], **Shilpak Chatterjee**[1,##], **Paulo C. Rodriguez**[8], **Eduardo N. Maldonado**[3], **J. Alan Diehl**[9], **Vamsi K. Gangaraju**[2], **Shikhar Mehrotra**[1,10,*]

[1]Department of Surgery, Hollings Cancer Center, Medical University of South Carolina, Charleston, SC 29425 (USA)

[2]Department of Biochemistry and Molecular Biology, Hollings Cancer Center, Medical University of South Carolina, Charleston, SC 29425 (USA)

[3]Department of Drug Discovery and Biomedical Sciences, Hollings Cancer Center, Medical University of South Carolina, Charleston, SC 29425 (USA)

[4]Department of Pathology & Laboratory Medicine, Hollings Cancer Center, Medical University of South Carolina, Charleston, SC 29425 (USA)

[5]Department of Cell and Molecular Pharmacology and Experimental Therapeutics, Hollings Cancer Center, Medical University of South Carolina, Charleston, SC 29425 (USA)

[6]Department of Neuroscience, Hollings Cancer Center, Medical University of South Carolina, Charleston, SC 29425 (USA)

[7]Department of Public Health, Hollings Cancer Center, Medical University of South Carolina, Charleston, SC 29425 (USA)

[8]Department of Immunology, H. Lee Moffitt Cancer Center & Research Institute, Tampa, FL 33612, USA

[9]Department of Biochemistry, Case Western University, 10900 Euclid Avenue, Cleveland, OH 44106, USA

[#]Co-corresponding author.

[##]current address: CSIR-IICB Translational Research Unit of Excellence, CN-6, Salt Lake, Sector V, Kolkata – 700091, India

[*]Lead contact: Shikhar Mehrotra, Ph.D., Department of Surgery, Hollings Cancer Center (HO 512H), Medical University of South Carolina, 86 Jonathan Lucas Street, Charleston, SC 29425, USA, Phone: 843-792-9195; FAX: 843-792-2556; mehrotr@musc.edu

Author Contributions: *Conception and design*: PC, SM. *Development of methodology*: PC, RYP, SC, DT, MG, DSK, DP, IK, SC. *Acquisition of data (provided animals, acquired and managed patients, provided facilities, etc.)*: PC, RYP, SC, DT, MG, ZTH, DSK, DP, IK, LB, SC. *Analysis and interpretation of data (e.g., statistical analysis, biostatistics, computational analysis)*: PC, RYP, MG, SNN, GCB, SB, VP, HW, HL, EM, PCR, JAD, VKG, SM. *Writing, review, and/or revision of the manuscript*: PC, RYP, MM, HW, HL, JAD, VKG, SM. *Administrative, technical, or material support (i.e., reporting or organizing data, constructing databases)*: PC, RYP, HL, VKG, SM. *Study supervision*: SM.

COI statement: Shikhar Mehrotra is co-founder and Chief-Scientific Officer of LipoImmuno Tech, LLC. The authors declare that they do not have any conflicting financial interests with this work.

Author Manuscript Author Manuscript Author Manuscript Author Manuscript

[10]Department of Microbiology & Immunology, Hollings Cancer Center, Medical University of South Carolina, Charleston, SC 29425 (USA)

[11]Department of Clinical Chemistry and Biochemistry, Medical University of Lodz, 60 Narutowicza St. 90-136 Lodz, Poland

Abstract

Mitochondria and endoplasmic reticulum (ER) share structural and functional networks and activate well-orchestrated signaling processes to shape cells' fate and function. While persistent ER stress (ERS) response leads to mitochondrial collapse, moderate ERS promotes mitochondrial function. Strategies to boost anti-tumor T-cell function by targeting ER-mitochondria crosstalk have not yet been exploited. Here, we used carbon monoxide (CO), a short-lived gaseous molecule, to test if engaging moderate ERS conditions can improve mitochondrial and anti-tumor functions in T cells. In melanoma antigen-specific T cells, CO-induced transient activation of ERS sensor protein kinase R-like endoplasmic reticulum kinase (PERK) significantly increased anti-tumor T-cell function. Furthermore, CO-induced PERK activation temporarily halted protein translation and induced protective autophagy, including mitophagy. The use of LC3-GFP enabled differentiation between the cells that prepare themselves to undergo active autophagy (LC3-GFP^{pos}) and those that fail to enter the process (LC3-GFP^{neg}). LC3-GFP^{pos} T cells showed strong anti-tumor potential, whereas LC3-GFP^{neg} cells exhibited a T regulatory-like phenotype, harbored dysfunctional mitochondria, and accumulated abnormal metabolite content. These anomalous ratios of metabolites rendered the cells with a hypermethylated state and distinct epigenetic profile, limiting their anti-tumor activity. Overall, this study shows that ERS-activated autophagy pathways modify the mitochondrial function and epigenetically reprogram T cells towards a superior anti-tumor phenotype to achieve robust tumor control.

Keywords

T cell; Immunometabolism; Epigenetics; Melanoma; ER stress

INTRODUCTION

Adoptive cell transfer (ACT) is a powerful immunotherapeutic tool against cancer. Yet, the long-term control of established tumors has not been achieved due to various regulatory factors present in the tumor microenvironment (TME) (1). Among these, repeated and chronic antigenic stimulation, nutrient deprivation, presence of an immunosuppressive population in the TME are the key factors that attenuate T cell response after ACT and confer them with an increasingly exhausted and senescent phenotype (1). This leaves substantial room for improving the outcome of ACT.

Mitochondrial function plays a vital role in maintaining robust effector function, longevity, and fitness of anti-tumor T cells (2). Several studies established that adoptively transferred T cells' persistence and anti-tumor potential depend on their enhanced mitochondrial function (3). Various strategies to increase mitochondrial fitness of anti-tumor T cells are being tested to improve the persistence and get a durable and effective benefit(2–4). The development

Author Manuscript Author Manuscript Author Manuscript Author Manuscript

in T cell immunotherapies over the past decade has also revealed that the reinvigoration of anti-tumor immunity can be achieved by manipulating mitochondrial dynamics in T cells (2,5,6).

Almost all cellular compartments (including the plasma membrane, endosomes, and peroxisomes) dynamically coordinate with ER to maintain normal cellular function. However, mitochondria play the most crucial role in regulating cell metabolism and death (7). It has been reported that the early phase of ER stress induces mitochondrial biogenesis (7) and enhances mitochondrial respiration by $Ca2^{+}$ transfer (8). However, persistent ER stress response leads to mitochondrial collapse, ultimately turning on apoptotic cell death mechanisms (7). Over the years, several studies showed that hostile conditions in the TME, including ROS, hypoxia, and nutrient deprivation, alter ER homeostasis in T cells, leading to severe mitochondrial and T cell dysfunctionality (9–12). On the contrary, other reports showed that activation of ERS sensor pathways plays a critical role in T cell differentiation and NK cell function (13–15). Thus, it remains unclear how the duration of ERS modulates the functionality of mitochondria and therefore impacts the anti-tumor property of T cells.

Carbon monoxide (CO) is an endogenous gaseous molecule considered a ‘silent killer’ due to its deleterious effects on the brain. However, it also functions as a neurotransmitter and regulates numerous cellular processes (16). Emerging evidence also suggests that low-dose CO exposure is beneficial in cellular processes based on anti-apoptotic, anti-inflammatory, antithrombotic, anti-fibrotic effects (16,17). Furthermore, several reports showed that CO treatment activates ERS sensor pathways and increases mitochondrial biogenesis in various cell types (18,19). The therapeutic effects of low-dose CO led to numerous ongoing clinical trials in different disease models (16,19). However, presently, it remains unexplored if low-dose CO exposure regulates the ERS signaling and enhances mitochondrial function and metabolism in T cells in the context of ACT.

This study determined if low-dose CO exposure influence the ER-mitochondria crosstalk to govern the T cells’ fate and function in an adoptive T cell transfer model. Here we report that CO-induced transient activation of ER stress sensor molecule PERK temporarily halts protein translation, induces mitochondrial biogenesis and protective autophagy as a survival mechanism in $CD8^{+}$ T cells. Furthermore, autophagy activation drives distinct metabolic and epigenetic reprogramming in T cells, ultimately programming them as a superior effector with enhanced anti-tumor function. We believe that immunometabolic reprogramming of anti-tumor T cells with a gaseous molecule like CO would be highly advantageous to not only obtain long-term tumor control but drastically reduce the cost of ACT.

MATERIALS AND METHODS

Mice

C57BL/6, B6-HLA-$A2^{+}$, B6-$Rag^{-/-}$, Pmel, CAG-RFP-EGFP-LC3 reporter mice were obtained from Jackson Laboratory (Bar Harbor, ME). These mice express the tamoxifen-inducible Cre-ERT2 fusion protein (Cre-ERT2) under the control of the promoter/enhancer regions, $PERK^{fl/fl}$ $ERT2^{cre}$ mice were a kind gift from Dr. Alan Diehl (Case Western University). In addition, Pmel-RFP-EGFP-LC3 and h3T-RFP-EGFP-LC3 mice knock-in

Author Manuscript Author Manuscript Author Manuscript Author Manuscript

mice were developed in the lab. Animals were maintained in pathogen-free facilities, and experimental procedures were approved by the Institutional Animal Care and Use Committees of Medical University of South Carolina, Charleston. For tumor experiments, an equal number of age- and gender-matched (both male and female) mice were randomly assigned for the experiments when they were between 8–10 weeks old. No influence of sex on the result of the studies was observed.

Cell Lines

B16-F10 and 624-MEL were obtained from American Type Culture Collection (ATCC), suggesting male origin.

T cell differentiation

Naïve total T cells were purified from the total splenocytes of 6–9-week-old WT (C57BL/6) and KO ($PERK^{fl/fl}ERT2^{cre}$) mice, first by incubating the cells with biotinylated anti-CD19, anti-Gr1, Anti-Mouse TER-119, anti-CD11b, anti-CD11c, anti-NK1.1, anti-CD25, anti-CD105 (cell signaling technology), followed by negative selection with streptavidin magnetic particles (BD Biosciences). Total splenocytes from 6–9-week-old TCR transgenic mouse Th0 (100 IU/ml IL2) in the presence of plate-bound anti-CD3 (2 μg/ml) and anti-CD28 (5 μg/ml). Pmel (bears Class-I restricted $CD8^+$ T cells) were also used. Within experiments, mice were age and sex-matched. For Pmel TCR transgenic mice, splenocytes were stimulated with 1 μg/ml gp100 melanoma antigen in the presence of 100 IU/ml IL2. T cells were differentiated for three days in IMDM media supplemented with 10% FCS, 4mM L-glutamine, 100 U/ml penicillin, 100 μg/ml streptomycin, 55μM beta-mercaptoethanol under 5% CO_2, atmospheric oxygen at 37°C in a humidified incubator. T cells were re-stimulated to evaluate intracellular cytokines by flow cytometry either with PMA/ionomycin for four hours or plate-bound anti-CD3 (5 μg/ml) and anti-CD28 (5 μg/ml) or with gp100 melanoma antigen for overnight in the presence of Golgi inhibitors. In some experiments, *in vitro* differentiated T cells were either treated with the vehicle control or inhibitor of IRE1α, 4μ8c (15 μM; or inhibitor of PERK, GSK2606414 (1μM) or inhibitor of Autophagy 3-Methyladenine (3-MA) (5 mM) for 48 hours.

Retroviral Transduction

One day before transfection, 5×10^6 Platinum-E ecotropic packaging cells (Cell Biolabs) were seeded in 10 mL antibiotic-free medium in 100 mm dishes (Corning). Packaging cells were transfected with 18 mg retroviral plasmid DNA encoding either TIL 1383I TCR or PPARγ empty/WT/mutant vector and the helper plasmid pCL-Eco using 36 mL Lipofectamine 2000 in OptiMEM (Invitrogen). After 24hr, the medium was replaced, and the cells were incubated for an additional 24hr, after which the retrovirus-containing supernatant was collected and filtered. The viral supernatant was spun at 2,000g for 2 hr at 30 °C onto non-tissue-culture-treated 24-well plates (USA Scientific) coated overnight with Retronectin. Freshly isolated mouse $CD8^+$ T cells were activated with CD3/CD28-coated beads (Dynabeads, Life Technologies) at a 1:1 bead: cell ratio along with either T cell differentiation media (as described above) or IL2 containing media (100 U/ml) the same day as packaging cell transfection. Beads were removed 48 hr post-activation, just before transduction, and re-suspended to a concentration of 2×10^6 cells ml-1 in a fresh medium.

Author Manuscript Author Manuscript Author Manuscript Author Manuscript

After removing the virus from the Retronectin-coated plate following the first spin, 1 mL of the activated T cells were then plated in the same wells, and 1 mL of the fresh virus was added on top of the cells. The plate was spun for an additional 2 h at 1100g, 32 °C. Post-spin, 1 mL of media was removed and replaced with fresh media containing 200 IU/ml IL-2 before the cells were incubated overnight. The cells were collected, washed, and plated the following day at 10^6 cells/ml.

Adoptive T cell protocol

B16-F10 (0.3×10^6) or B16-F10-$A2^+$ Or 624-MEL (2.5×10^6) melanoma tumor cells were injected subcutaneously (*s.c.*) into left flank of 8–10-week-old C57BL/6 or HLA-$A2^+$ or NSG mice respectively. After tumor establishment, recipient mice were injected *(i.p*) with cyclophosphamide (4 mg/mice) before adoptively transferring (i.v) either Pmel ($CD8^+V\beta13^+$) or h3T ($CD8^+V\beta12^+$) or TIL1383I TCR^+ cells. After adoptive T cell transfer. Recipient mice were given IL2 (50,000 U/mouse; i.p) for three consecutive days after ACT.

Flow cytometry

Staining for cell surface markers was performed by incubating cells with the antibody at 1:200 dilutions in FACS buffer (0.1% BSA in PBS) for 30 min at 4°C. For intracellular cytokine (IFNγ and IL17a) and Sphk1 staining, surface markers were stained before fixation/permeabilization (BD Cytofix/Cytoperm Kit, BD Biosciences, San Jose, CA). For staining of transcription factors, cells were stained with surface markers and fixed/permeabilized with a FoxP3 staining buffer set (eBioscience, San Diego, CA). For pIRE1α and pPERK staining, cells were fixed/permeabilized using BD perm III buffer set (BD Bioscience, San Jose, CA) before staining with cell surface markers and pIRE1α or pPERK primary antibody (Cell Signaling Technologies, Danvers, MA), followed by fluorochrome-conjugated secondary antibody (Jackson ImmunoResearch Laboratories, West Grove, PA). In addition, CaspGLOW™ Fluorescein Active Caspase-3 Staining Kit (Invitrogen # 88-7004-42), MitoTracker® Red (Cell signaling technology #9082), LIVE/DEAD™ Fixable Yellow Dead Cell Stain Kit (Invitrogen # L34959), and CYTO-ID® Autophagy detection kit (Enzo # ENZ-51031-0050) were used to evaluate Caspase-3 activity, mitochondrial mass, cell death, and autophagy respectively following manufacturer's protocol. Samples were acquired on LSRFortessa and analyzed with FlowJo software (Tree Star, OR).

Real-time quantitative-PCR

Total RNA was extracted from pellets of the indicated T cell subsets (2×10^6 cells) using Trizol reagent (Life Technologies, Grand Island, NY). cDNA was generated from 1 μg total RNA using iScript cDNA Synthesis Kit (BioRad, Hercules, CA). SYBR Green incorporation quantitative real-time PCR was performed using an SYBR Green mix (Biorad, Hercules, CA) in the CFX96 Detection System (BioRad, Hercules, CA). The expression of different genes was quantified relative to *Actb.*

Immunoblotting

For evaluation of the protein level, cell pellets were washed in PBS and lysed in RIPA buffer (Thermo Fisher Scientific, Waltham, MA), including protease/phosphatase inhibitors,

Author Manuscript Author Manuscript Author Manuscript Author Manuscript

vortexed, and incubated for 20 minutes on ice. Cell lysates were then centrifuged at 12,000 rpm for 15 min at 4°C. The supernatants were collected, and proteins were quantified with a BCA protein assay kit (Thermo Fisher Scientific, Waltham, MA). For immunoblot analyses, 20 μg of protein lysates per sample were denatured in 4X Loading dye and boiled using a heating block at 95 degrees for 10 minutes before loading to SDS gradient gels 4%−20% (Bio-Rad Criterion, 1h runs). Gels were semi-dry transferred onto PVDF, and the membranes were blocked with 3% milk in 0.1% TBST. The membraneNext, the membrane was probed with either PGC1 α antibody (Millipore Sigma, Burlington, MA), PERK antibody (Novus Biologicals, Centennial, CO), Phospho-IRE1 α (Ser724) antibody (Invitrogen, Waltham, MA), MFN2, OPA1, Phospho-PERK (Thr980), IRE1 α, LC3A/B antibody (Cell Signaling Technology, Danvers, MA), or β-Actin antibody (Santa Cruz Biotechnology, Inc, Dallas, TX) overnight at 4°C followed by one-hour incubation with HRP-conjugated secondary antibody (Cell Signaling Technology, Danvers, MA) and using a Clarity Western ECL Substrate (Bio-Rad, Hercules, CA).

Transmission Electron Microscopy (TEM)

The cells were pelletized and fixed in 2% Phosphate Buffered Glutaraldehyde for one hr. Next, the pellets were rinsed in 0.1M Phosphate Buffered Rinse and then postfixed in 2% Aqueous Osmium Tetroxide for one hr. After rinsing in distilled water, the pellets were dehydrated through a series of graded Ethyl Alcohol; 50% ETOH for 15 min, 70% ETOH for 15 min, 95% ETOH for 15 min, and finally twice with 100% ETOH for 15 min each. The dehydrant was removed using the intermediate fluid, Propylene Oxide, one change of 10 min each. Next, the pellets were infiltrated with a 1:1 solution of propylene oxide and Embed 812 (Electron Microscopy Sciences, Ft. Washington, PA) for one hr. The infiltration was continued using a 1:2 solution of propylene oxide and Embed 812 overnight. The pellets were embedded in Embed812 the following day and polymerized in a 60°C oven for 48 hr. Preliminary 1/2-micron sections were cut and stained with Toluidine Blue and examined using a light microscope. Then with the cell types identified, the 70nm thin sections are cut and stained with uranyl acetate and led citrate and allowed to dry. The sections are viewed on the JEOL 1010, and images are taken with a Hamamatsu electron microscope camera.

Confocal Microscopy

Purified $CD8^+$ T cells obtained from Pmel /LC3-GFP-RFP mice were stimulated with αCD3 and αCD28 Ab for three days in IL2 (100 IU/ml). Cells were then transferred into gelatin-coated 35 mm glass-bottom MatTek dishes. CORM3 (100μM) was added to the culture media. After 24h, cells were loaded with MitoTracker Deep Red (200 nM: M22426) for 1.5 h to visualize mitochondria. After loading, cells were fixed using 4% paraformaldehyde. GFP and MitoTracker Deep Red fluorescence were imaged in a Zeiss LSM 880 NLO inverted laser scanning confocal microscope (Thornwood, NY) using a 63X 1.4 N.A. plan-apochromat oil immersion lens. LC3-GFP and MitoTracker Deep Red were excited at 488 nm and 633 nm, respectively. Emitted light was detected with an Airyscan super-resolution detector at BP 495–550 nm for GFP and LP 654 nm for MitoTracker Deep Red. Z-stack Airyscan images were processed using the Huygens Professional deconvolution and image analysis software (Scientific Volume Imaging, The Netherland). After images were deconvolved using Huygens' Deconvolution Express (Standard Profile)

Author Manuscript Author Manuscript Author Manuscript Author Manuscript

that determines optimal parameters, we performed surface rendering of deconvolved images without watershed augmentation to create 360° 3D movies of surface rendered images.

Metabolism Assays

Glucose uptake by ex vivo differentiated T cells was determined by incubating cells with 100 μM 2NBDG (Cayman Chemical, Ann Arbor, MI) for 30 minutes before measuring fluorescence by flow cytometry. Oxygen consumption rate (OCR) and extracellular acidification rate (ECAR) were determined using the Seahorse Xfe96 analyzer (Agilent Technologies, Santa Clara, CA). Briefly, T cells (0.5×10^6/well) were plated on a Cell-Tak coated Seahorse culture plate for 30 min. OCR, a measure of OXPHOS, was analyzed under basal condition, or in response to 1.0 μM oligomycin, 1.0 μM fluoro-carbonyl cyanide phenylhydrazone (FCCP) and 2 μM rotenone, plus 100 nM antimycin A. ECAR, a measure of glycolysis, was measured under basal conditions and in response to glucose (5.5 mM), Oligomycin (1.0 μM), and 2-deoxyglucose (2-DG) (100 mM). All reagents were purchased from Sigma-Aldrich, St. Louis, MO.

Metabolomics

Different metabolites' intracellular levels were determined by performing comprehensive hydrophilic metabolites analysis using LC/MS platform (Metabolomics Core Facility, Northwestern University). Data were then analyzed using MetaboAnalyst software. Samples were loaded equivalently across the platform and normalized to Bradford values before statistical analysis.

Measurement of ATP

ATP was measured with a commercially available kit (Luminescent ATP Detection Assay Kit (ab113849) using bioluminescence following the manufacturer's protocol.

Protein synthesis assay

T cells were incubated for 1 hour at 37 °C in methionine-free RPMI 1640 medium (Life Technologies) containing 10% FBS (R& D Technologies). Then Click-iT™ HPG Alexa Fluor™ 488 Protein Synthesis Assay Kit (Life Technologies) was used to measure protein translation using flow cytometry following the manufacturer's protocol.

Isolation of tumor-infiltrating T cells

To obtain tumor-infiltrating T cells (TILs) from subcutaneously established solid B16-F10 melanoma-bearing mice, tumors were excised, chopped finely using tweezers and scissors, and then digested with 2 mg/ml collagenase type IV (Stemcell Technologies, Vancouver, BC) for 45 min. The tumors were filtered through 70 cell strainers (BD Biosciences, San Jose, CA). The cell suspension was washed in culture medium twice by centrifugation at 1500 rpm for 10 min at 4°C. After the second wash, the cells were re-suspended in 6 ml PBS and layered carefully over 3 ml Ficoll-paque (GE Healthcare) followed by centrifugation at 1500 rpm for 30 min at room temperature. The enriched TILs obtained at the interface as a thin buffy layer were washed with PBS twice and finally re-suspended in FACS staining buffer for further staining procedures.

Author Manuscript Author Manuscript Author Manuscript Author Manuscript

RNA Sequencing

RNA was extracted using mirVana™ miRNA Isolation Kit following the manufacturer's protocol. Samples were then sent to Novogene Corporation Inc (Beijing, China) for sequencing. Data analysis was performed using Partek Flow. Unaligned reads were mapped to mouse genome mm10 using STAR (PMC3530905), and read mapping to each RefSeq transcript was quantified. Differential expression analysis was performed using DESeq2 (PMC4302049), and the p-value was set at 0.05 to identify statistically significant changes.

ATAC Sequencing

We performed ATAC-seq as described by Corces *et al.(20)* with modification as described below. For making ATAC-seq libraries, we used 25×10^3 sorted T cells and modified the concentration of the Tn5 enzyme for transposase reaction. Corces et al. showed that lowered concertation of their homemade Tn5 on mouse embryonic stem cells had no changes in data quality(20). We used Illumina Tn5 for transposase reaction; hence we optimized Tn5 concentration for making ATAC-seq libraries for a range of cells from 10×10^3 to 100×10^3 (Fig S1a). We found that 40% of recommended Tn5 concentration is sufficient for 25, 25×10^3 $CD8^+$ T cells and used that concentration for preparing all libraries in this study. Our modified transposase reaction mix contains, 25 µl 2x TD buffer, 1µl transposase, 16.5 µl PBS, 0.5 µl 1% digitonin, 0.5 µl 10% Tween-20, 6.5 µl H_2O. Sequencing was performed at Novogene Corporation Inc (Beijing, China). Data analysis was performed using Partek Flow. ATAC-seq: Sequencing adapters were trimmed from raw sequencing reads using Cutadapt. Reads shorter than 25 and those that mapped to mitochondrial genome were discarded. The remaining reads were mapped to the mouse genome (mm10) using BWA. After alignment, duplicate reads, low mapping quality, and more than 2 mismatches were discarded. Reads with the same starting position were treated as duplicate reads. Peaks were then identified using MACS2(21) with a q-value cut-off of 0.05 and a fold enrichment cut-off of 1. Peaks were then annotated, and reads mapping to transcription start sites, transcription termination sites, Intron, Exon, 5' UTR Exon, 3' UTR Exon, CDS Exon, and Intergenic regions were quantified. To be considered within a feature, a read was required to have a minimum of 80% overlap with the feature. Reads were then normalized as counts per million mapped reads to compare amongst biological replicates. Differential expression analysis was performed using Gene Specific Analysis (GSA), and the p-value was set at 0.05 to identify statistically significant changes.

Quantification and statistical analysis

All data reported are the arithmetic mean from at least three independent experiments performed in triplicate ±SD unless stated otherwise. The unpaired Student *t-test* was used to evaluate the significance of differences observed between groups, accepting $P < 0.05$ as a threshold of significance. Data analyses were performed using the Prism software (GraphPad, San Diego, CA). Data were analyzed using R packages. For all survival outcomes, Kaplan-Meier curves were used to display the results. Median survival time and corresponding 95% confidence interval were calculated for each experimental condition. A log-rank test was used to compare the outcomes across experimental conditions. For all continuous outcomes, graphical displays (*e.g.*, bar charts) were used to demonstrate

Author Manuscript Author Manuscript Author Manuscript Author Manuscript

patterns of the outcomes within and across experimental conditions. Normality and variance homogeneity assumptions were assessed, and appropriate data transformations were used. All continuous outcomes were measured longitudinally from the same animal. These measures were modeled using linear mixed-effects (LME) regression, including fixed effects for experimental condition, time, and their two-way interaction; subject-specific random effects were incorporated to account for the correlation among measures obtained from the same subject over time. Comparisons between conditions and times using model-based linear contrast with inference based on associated two-sided Wald tests adjusting multiple comparisons.

Contact for reagent and resource sharing

The reagents and resources used for the experiments have been described in Table 1 (key resource table). Further information and requests for resources and reagents should be directed to and fulfilled by the Lead Contact, Shikhar Mehrotra (mehrotr@musc.edu).

Data and software availability—Sequencing data have been deposited in the Gene Expression Omnibus (GEO) under accession number GSE197530.

RESULTS

CO-induced transient ERS sensor molecule activation enhances mitochondrial content and function in T cells.

To assess the role of low dose CO exposure on ER-mitochondria interaction in T cells, we used the carbon monoxide releasing molecule 3 (CORM3) (22). Along with CORM3 (referred to as CO hereafter), we used another ERS response pathway activator, namely Thapsigargin (TG) (23), to find out any CO-specific effect on ER-mitochondria signaling under a moderate level of ERS sensor molecule activation. To determine the non-toxic doses of CO and TG, melanoma epitope gp100 reactive T cells (from Pmel transgenic mouse) were activated with cognate antigen, and TG or CO were added for the last 48 hours of activation at different doses. After incubation, cells were stained with live/dead staining dye and analyzed by flow cytometry (Fig. 1a). We found that 10nM of TG and 100 μM of CO are non-toxic, whereas 100 nM TG and 200 μM CO caused significant cell death in T cells. Treatment with 100 μM CO and 10 nM TG for 48 hours does not trigger any apoptotic cell death pathway, as determined by flow-cytometry-based caspase-3 activation compared to their untreated counterpart (Fig. 1b). Brefeldin A (BFA) served as a positive control for caspase-3 activation(24) (Fig. 1b). Pmel T cells were then activated for 72 hours, and either TG or CO was added at the last 6h, 24h, and 48h of activation to evaluate the total expression and phosphorylated status (activated form) of different ER sensor proteins by flow cytometry (Fig. 1c), western blot analysis (Fig. 1d) and by qPCR analysis (Fig. S1b). We observed that TG and CO treatment (at their non-toxic doses) cause transient activation of PERK and IRE1α in Pmel T cells after 6h of treatment that declined at 24h (Fig. 1c). However, we saw a more prolonged chop expression after TG treatment (until 48h, the last time point observed) than CO in Pmel T cells (Fig. S1b). $CD4^+$ T cells obtained from C57BL/6 mice also showed similar kinetics as $CD8^+$ Pmel T cells (Fig. S1c). We did not see any significant changes in the spliced variant of XBP1 (sXBP1: downstream target of

Author Manuscript Author Manuscript Author Manuscript Author Manuscript

IRE1α) after CO or TG treatment (Fig. S1d, S1e). Next, we determined if TG and CO affect mitochondrial biogenesis and function. Both flow cytometry analysis data (Fig. 1e & Fig. S1f: MitoTracker Deep Red FM) and confocal microscopic picture (Fig. 1f: MitoTracker Red FM) show that CO exposure and TG treatment leads to enhanced MitoTracker Deep Red fluorescence. MitoTracker Red is not specific to determine mitochondrial mass because the uptake of the dye is influenced by mitochondrial membrane potential, which can vary from cell to cell, or within the same cell, leading to a differential uptake. However, the increase in MitoTracker Red fluorescence was consistent with an increase in the expression of genes associated with mitochondrial biogenesis (Fig. 1g & 1h), strongly suggesting an increase in mitochondrial mass induced by CO and TG. To gain insight into mitochondrial function, respiration in Pmel T cells cultured either in the presence or absence of CO and TG was assessed in a real-time flux assay. Compared to untreated counterparts, both TG and CO treated Pmel T cells exhibited increased basal respiration, maximal respiratory capacity, and spare respiratory capacity. In addition, both treatments increased oligomycin-sensitive respiration (Fig. 1i). Together, this data suggests that moderate ERS sensor activation leads to higher mitochondrial mass and function in T cells.

CO treatment improves T cell effector function and anti-tumor property *in vivo*.

Studies from different groups showed elevated mitochondrial activity in T cells could positively impact survival, self-renewal property, and the rapid transition to effector phenotype generation after antigen re-exposure (2,3). Thus, we determined the expression of stemness markers in TG or CO-treated cells. Both CO and TG-treated Pmel T cells exhibited increased cell surface expression of stem cell antigen (Sca1), CD27, and CD28 than untreated T cells (Fig. 2a). Treating Pmel T cells with TG and CO also increased the expression of stemness-associated genes, such as *Tcf7*, *oct4*, *Nanog*, and *β-catenin* (Fig. 2b). Upon restimulation with cognate antigen, TG-treated cells displayed less granzyme B (GzmB) and IL2 but more IL10 production than untreated Pmel T cells (Fig. 2c and Fig. S1g). On the contrary, CO-treated T cells showed enhanced IFNγ, IL2, and GzmB (Fig. 2c and Fig. S1g) production. Reduced effector function displayed by TG-treated T cells led us to choose CO for future investigation.

Next, we determined if CO treatment rendered T cells with enhanced capacity to survive *in vivo*. Thus, 3-day antigen-activated Pmel or CO-treated Pmel T cells into $Rag1^{-/-}$ mice were transferred adoptively. After 25 days, recipient mice were injected with murine melanoma B16-F10 cells (Fig. S2a). Five days' post tumor injection, CO-treated T cells exhibited a higher recall response to tumor challenge than Pmel T cells, as evident from their 2-fold higher expansion in each organ (Fig. S2b). This was also supported by enhanced effector cytokine (IFNγ and TNFα) levels by CO-treated T cells retrieved from the spleen and draining lymph nodes (DLNs) (Fig. S2c). Further, B16-F10 melanoma tumor cells (0.3×10^6) were subcutaneously established into C57BL/6 recipient mice for nine days. After that, the recipient mice were injected (*i.p*) with cyclophosphamide before Pmel T cells (either CO treated or untreated) were adoptively transferred into the tumor-bearing mice. As shown in Fig. 2d, the tumor progression was significantly slower and overall survival was improved (Fig. S2d) in recipient mice that received CO-treated T cells than those administered with untreated T cells, suggesting that CO signaling improved T cells cell-mediated anti-tumor

Author Manuscript Author Manuscript Author Manuscript Author Manuscript

immune response. We also examined tumors, DLNs, and spleens harvested from the mice adoptively transferred with Pmel or CO treated Pmel. A significantly higher number of gp100 reactive T cells were retrieved from tumor sites and DLNs (Fig. 2e and Fig. S2e). The retrieved Pmel T cells from the tumor site and DLNs also retained their glycolytic activity (Fig. 2f and Fig. S2f), mitochondrial mass (Fig. 2g and Fig. S2g), secreted significantly higher amount of effector cytokine-like IFNγ, TNFα, GzmB (Figs. 2h, 2i, S2h, and S2i), and expressed less amount of different inhibitory markers like PD1, TIM3, Lag3 (Fig. 2j and Fig. S2j *(gating strategy,* S2k *(MFI values),* S2l *(percentage of total Vβ13$^+$CD8$^+$ T cells)*) when the mice received CO treated T cell transfer. Next, to find out the differences in T cell activation and differentiation status of tumor retrieved T cells, we checked the expression of surface molecules and transcription factors implicated in identifying T cell exhaustion status (25,26). A significant decrease in the terminally exhausted PD1$^+$Tim3$^+$ (Fig. 2k and S2m) and an increase in the stem-like PD1$^+$TCF1/7$^+$ (Fig. 2l and S2n) was observed in the gp100 reactive T cells retrieved from mice adoptively transferred with CO treated T cells. We did not see any significant changes PD1$^+$Cx3Cr1$^+$ transitory population (Fig. 2m and S2o), whereas the PD1$^+$CD44$^+$ subset was increased (Fig. 2n and S2p) in adoptively transferred CO treated Vβ13$^+$CD8$^+$ T cells. Together the data suggest that CO-treated T cells mediated long-term tumor control might be caused by the stem-like cells PD1$^+$TCF1/7$^+$ population.

In an ideal translational scenario for the ACT, the peripheral blood-derived T cells from a tumor-bearing patient will need to be engineered (with tumor epitope reactive TCR or CAR), or tumor-infiltrating lymphocytes (TILs) isolated from the patient's tumor will have to be expanded *ex vivo* before autologous ACT (27,28). Thus, we isolated TILs from murine B16-F10 tumors or used human TILs (lung tumor) and exposed them to CO. We observed a substantial increase in mitochondrial mass and effector cytokine production for both mice (Fig. 2o) and human TILs (Fig. 2p) compared to their untreated counterpart. These data suggest that CO-mediated transient ERS activation (*in vitro*) enhances effector function and could rescue the tumor-reactive T cells from their dysfunctional state in TME.

CO-mediated mitochondrial biogenesis is dependent on PERK activation.

Next, we sought to determine which ER stress sensor pathway is responsible for enhanced mitochondrial function in CO-exposed T cells. Thus, Pmel T cells were pretreated with pharmacological inhibitors of IRE1α (4μ8c) (29), and PERK (GSK2606414) (30) pathway before being treated with CO, and mitochondrial fitness was determined. Pharmacological inhibition of PERK, but not IRE1α, reduced mitochondrial mass in CO-treated T cells (Fig. 3a), indicating the PERK pathway in CO-mediated mitochondrial biogenesis. This result was confirmed using PERK-KO T cells upon staining with Mito Red FM (Fig. 3b). Transmission electron microscopy images - showed swollen mitochondria and disorganized cristae in PERK-KO T cells compared to condensed cristae in CO-treated T cells (Fig. 3c). Corroborating this, we observed that PERK-KO T cells significantly lost mitochondrial respiration and ATP production, both at the base level and under the stressed condition, as evident from the real-time flux assay (Fig. 3d). Furthermore, CO-treated PERK-KO T cells engineered with melanoma epitope tyrosinase reactive TCR TIL1383I failed to control the growth of murine melanoma B16-A2 upon adoptive transfer (Fig 3e). Overall, this data

Author Manuscript Author Manuscript Author Manuscript Author Manuscript

indicates that CO-mediated transient activation of PERK signaling renders metabolic fitness to T cells, resulting in robust T cell-mediated tumor control.

Activation of PERK signaling has been shown to inhibit general protein translation *via* eIF2α phosphorylation(7). Given that the extent of overall translation in activated T cells strongly correlates with cell proliferation, memory T cell generation, and effector function in TME (31,32), we next determined if transient PERK activation impacts the translation machinery of activated Pmel T cells. Thus, Pmel T cells were activated for 72 hours, and CO was added at the last 24h and 48h of activation. We noticed an upregulation in eIF2α phosphorylation (inhibits global protein translation) after CO treatment (Fig. 3f). To compare the extent of protein synthesis in CO treated and untreated T cells, we assessed the incorporation of L-homopropargylglycine (HPG), a non-radioactive amino-acid analog of methionine that can be measured by flow cytometry (31). Since memory T cells have been shown to reduce translation (31), IL-15 treated T cells were also included in the experiment. We noted that overall translation is less in CO treated and IL-15 treated T cells (less incorporation of HPG) than untreated (IL-2 treated) T cells. However, both CO and IL-15 treated T cells substantially upregulate the incorporation of HPG after antigenic restimulation (Fig. 3g), indicative of increased protein synthesis. This was further supported by finding that both CO and IL-15 treated T cells produce markedly high effector cytokines in response to minimal antigen re-exposure (Fig. 3h, and S3a). We next determined the role of PERK signaling in CO and IL15 mediated temporary blockade of protein translation. The HPG incorporation data displayed that CO-treated T cells do not upregulate HPG incorporation in response to antigen restimulation in PERK-KO T cells (Fig. S3b). However, the absence of PERK does not hamper IL15 mediated increase in protein translation after antigen restimulation (Fig. S3b). These *in vitro* results prompted us to examine whether CO pretreated Pmel T cells regain their protein translation activity in tumor-bearing mice after homeostatic proliferation. To this end, we transferred untreated (only IL2), CO treated, or IL15 treated Pmel T cells into $Rag1^{-/-}$ mice. After 25 days, the recipient mice were injected with B16-F10 cells (1×10^4 cells/mouse) to stimulate proliferation. Five days later, tumor-reactive T cells were collected (from DLNs), and translation activity was measured on a fraction of the retrieved cells. The rest were sequentially transferred to a new set of tumor-bearing $Rag1^{-/-}$ hosts, tumor-specific T cells were recovered from tumors, and translation activity was measured (Fig. 3i). Though we did not see any significant difference in differentially treated groups after the first transfer, both IL15 and CO primed Pmel T cells enhanced translation relative to IL2 treated Pmel T cells after the second transfer in tumor-bearing hosts (Fig. 3j). Collectively our data indicate that transient ERS condition temporarily abrogates protein synthesis in T cells, indicating that robust and long-term anti-tumor effector function of CO pretreated Pmel T cells is likely associated with their "translationally-paused phenotype" *in vitro* and then activation of translation machinery in response to the TME.

Transient PERK activation improves tumor control by engaging autophagy.

We next questioned how transient activation of PERK signaling enhances mitochondrial function in CO-exposed T cells. Several studies showed that cells activate well-orchestrated cellular signaling processes to resolve ER stress. Many reports also indicate that autophagy

Author Manuscript Author Manuscript Author Manuscript Author Manuscript

is a pro-survival mechanism responding to low or moderate ERS to prevent cell damage(33). Autophagy has shown to be a quality control mechanism that maintains a healthy and functional mitochondrial network, and cells that do not undergo autophagy inherit damaged mitochondria. Additionally, exposure to CO is shown to induce autophagy (34–36). To determine if CO mediated transient ERS signal induces autophagy in Pmel T cells, we used a specific autophagosome detection reagent Cyto-ID (37). To determine the kinetic changes in autophagosome formation at different hours, $CD8^+$ or $CD4^+$ T cells were activated for 72 hours, and CO was added at the last 6h, 24h, and 48h of activation. Both $CD8^+$ and $CD4^+$ T cells displayed an accumulation of autophagosomes at the early hour of CO treatment (peaks at 24 hours) (Fig. 4a and Fig S4a), and then sequentially decreased after 48 hours of CO treatment (Fig. 4a and Fig S4a), suggesting an active autophagic flux after 48 hours. We also found a significant increase in the autophagy-associated genes after CO treatment. (Fig. 4b). The microtubule-associated proteins LC3bI and LC3bII (a lipidated form of LC3bI)(38) were also induced after CO treatment of $CD8^+$ T cells (Fig. 4c), indicating their incorporation into the early autophagosomes. To follow the autophagic flux in live T cells, we used CAG-RFP-EGFP-LC3 reporter mice that have CAG promoter/enhancer sequences driving expression of a red fluorescent protein (RFP), an enhanced green fluorescent protein (EGFP), and a microtubule-associated protein 1 light chain 3 alpha (Map1lc3a or LC3) gene. Co-expression of two fluorophores allows tracking different phagocytic cellular compartments depending on the environment's acidity. RFP is stable in acidic pH, while EGFP is quenched in the acidic lysosomal environment, allowing autophagosomes to be distinguished from autolysosomes (37,39). Combined GFP and RFP fluorescence yield a yellow signal within high pH phagophores and autophagosomes, while EGFP is quenched in autolysosomes, emitting only an RFP signal. To study the autophagic activity in an antigen-specific manner, melanoma epitope gp100 reactive Pmel-C57BL6/LC3-GFP-RFP mice were generated. Pmel/LC3-GFP-RFP T cells showed a slightly enhanced yellow signal ($GFP^{pos}RFP^{pos}$) at the early hours of CO exposure (24h), indicating an increase in total LC3 in preparation for autophagy in the initial hour (Fig. 4d). In contrast, a reduction in yellow signal and growth in the $GFP^{neg}RFP^{pos}$ proportion of cells (lower right quadrant) were observed in the late hours (48h), suggesting the quenching of GFP signals in autolysosomes and an ongoing autophagic flux (Fig. 4d). Next, we assessed the involvement of PERK activation to stimulate autophagy in CO-treated T cells. We observed a continuous increase in cyto-ID staining until 48 hours in CO-treated PERK-KO T cells, indicating an accumulation of autophagosomes and defects in autolysosome formation. (Fig. 4e). We also found that CO treatment stimulates Caspase-3 activation in PERK-KO T cells after 48 hours of treatment (Fig. 4f), most likely because the absence of autophagy (survival mechanism) cells trigger the death pathway. However, we did not observe any active cell death in CO-treated WT T cells until 48 hours.

Next, our flow cytometry data demonstrated that Mito Red FM signal intensity does not increase until 24 hours of CO treatment (Fig. 4g), suggesting that an active autophagic process (more specifically mitophagy) might be going on until 24 hours of treatment to replace the old dysfunctional mitochondria with healthy mitochondria. To get a closer look at mitophagy, Pmel /LC3-GFP-RFP T were loaded with MitoTracker Deep Red. Confocal images were taken after 24 hours of CO treatment (mitochondrial network is red and

Author Manuscript Author Manuscript Author Manuscript Author Manuscript

autophagy in green). Deconvolved and surface rendered images of untreated cells showed small and evenly distributed GFP-positive vesicles (Fig. 4h; *left panel*), whereas CO treated cells showed significant, high fluorescence intensity GFP-positive vesicles attached to and surrounding mitochondria (Fig. 4h; *right panel*).Furthermore, our western blot analysis data showed that CO treatment upregulates the expression of Atg3 and BNIP3 (Fig. 4i), two key proteins previously shown to be essential for mitophagy in NK cells(38). However, it failed to do so in PERK-KO T cells (Fig. 4i). Next, to confirm the role of autophagy in T cells' mitochondrial function, we treated Pmel T cells with CO either in the presence or absence of 3MA, a known autophagy inhibitor (40). The real-time flux analysis data revealed that autophagy inhibition significantly reduced mitochondrial respiration and ATP production at the base and under stressed conditions (Fig. 4j and Fig. S4b). Further, 3MA pretreated and CO-exposed Pmel T cells were transferred into B16-F10 melanoma bearing C57BL/6 recipient mice and monitored for tumor growth. As shown in Fig. 4k and Fig. S4c, CO-treated Pmel T cells significantly lost their anti-tumor function in the presence of autophagy blocker 3MA. Together these data indicate the role of transient PERK activation to induce autophagy as a cytoprotective mechanism to preserve healthy mitochondrial function in T cells. Next, we transduced WT T cells either with an empty construct or a PERK overexpressing construct to understand how continuous PERK signaling impacts mitochondrial function in T cells. However, we found that PERK overexpression in T cells triggers caspase-3 activation, resulting in massive cell death (Fig. S4d).

Cytoprotective autophagy contributes to healthy mitochondrial function and preserves vital anti-tumor effector function.

To get further insight into how autophagy impacts T cell fate and function, we decided to characterize the T cells based on their capacity to activate autophagic machinery in response to moderate ERS conditions. For this purpose, we used LC3-GFP as a marker to delineate between two T cell subsets, viz. cells that increase total LC3 expression to enter into the autophagic process (Pmel-LC3-GFP^{pos}), and who fail to do so (Pmel-LC3-GFP^{neg} T cells). To this end, Pmel-LC3-GFP-RFP T cells were activated, and CO was added at the last 24 hours of activation (when we obtained the highest percentage of LC3-GFP^{pos} T cells; Fig. 5a), and then LC3-GFP^{pos} and LC3-GFP^{neg} T cells were FACS sorted. Since our findings revealed that blocking autophagy using 3MA hampers mitochondrial function in T cells, we examined if any difference exists between LC3-GFP^{pos} and LC3-GFP^{neg} T cell subsets about mitochondrial structure and function. We did not observe any difference in mitochondrial structure studied by transmission electron microscopy. However, we observed substantial differences in the mitochondrial content between LC3-GFP^{pos} and LC3-GFP^{neg}T cell subsets (Fig. 5b). Furthermore, the real-time flux data revealed that OXPHOS under basal conditions and in response stress conditions was remarkably higher in the LC3-GFP^{pos} T cells than LC3-GFP^{neg} T cells, indicating an elevated mitochondrial function in LC3-GFP^{pos} T cells (Fig. 5c). In line with this, mitochondria energy metabolism array data showed that the genes associated with mitochondrial electron transport chains and antioxidant genes (protect cells from the detrimental effect of reactive oxygen species generation) were upregulated in LC3-GFP^{pos} T cells compared to LC3-GFP^{neg} T cells (Fig. 5d, Fig. S5a).

Author Manuscript Author Manuscript Author Manuscript Author Manuscript

Recently, mitochondrial defects (loss of cristae structure, mtDNA release, decreased OXPHOS) have been implicated in the production of IL-10 and Treg suppressive activity (41). Therefore, to study the functional relevance of mitochondrial dysfunction due to loss of autophagic activity, sorted subsets of T cells were restimulated in an antigen-specific manner, and effector cytokine production was measured. As a result, we noticed a markedly higher secretion of critical anti-tumor cytokines like IFN-γ and IL-9 by Pmel-LC3-GFP^{pos} T cells. Whereas Pmel-LC3-GFP^{neg} T cells secreted high levels of immunoregulatory IL-10 without any *ex vivo* programming (Fig. 5e). Next, RNA-seq was performed to identify the molecular signature of Pmel-LC3-GFP^{pos} and LC3-GFP^{neg} T cells. The data revealed distinct gene signatures of these two subsets (Fig. S5b and Fig. S5c). Notably, a higher expression of the TGFβ signaling pathway genes was observed in LC3-GFP^{neg} T cells (Fig. 5f). In line with this, Pmel-LC3-GFP^{pos} T cells exhibited higher production of effector cytokine (IFN-γ, GzmB) in the presence of TGFβ (Fig. 5g) and reduced Treg signature transcription factor FoxP3 expression (Fig. 5h) compared to Pmel-LC3-GFP^{neg} T cells, indicating that they might be susceptible to suppression in the TME.

We further determined if LC3-GFP can be used as a marker of 'metabolically fit' T cells in the context of autologous ACT (27,28). Thus, we isolated TILs from murine B16-F10 tumor-bearing Pmel/LC3-GFP-RFP mice and expanded them with TCR activation in the presence or absence of CO. We found that, upon TCR stimulation, CD8^{+} TILs start to express LC3-GFP. With CO exposure, the percentage of the LC3-GFP^{pos} population was significantly increased in TILs (Fig. S5d). To determine if LC3-GFP^{pos} and LC3-GFP^{neg} CD8^{+} TILs show similar phenotypes like LC3-GFP^{pos} and LC3-GFP^{neg} T cells, we restimulated them in an Ag-specific manner. As evident from Fig. S5e *(upper panel)* IFN-γ, Gzmb production was significantly higher in the LC3-GFP^{pos} compared to LC3-GFP^{neg} CD8^{+} TILs. Conversely, LC3-GFP^{neg} CD8^{+} TILs cells secreted high levels of immunoregulatory IL-10, expressed higher TGFβRII and FoxP3 (Fig. S5e *bottom panel*). To test if this reflects in their tumor control capacity, purified Pmel-LC3-GFP^{pos}, and Pmel-LC3-GFP^{neg} T cells were transferred into B16-F10 melanoma bearing C57BL/6 recipient mice. As shown in Fig. 5i, the tumor progression is significantly slower where the mice received Pmel-LC3-GFP^{pos} T cells transfer. Furthermore, some of the recipient mice which received Pmel-LC3-GFP^{pos} T cells transfer even showed tumor-free survival for an extended period suggesting a robust and long-lived effector response by anti-tumor Pmel-LC3-GFP^{pos} T cells. Importantly, when rechallenged with the same tumor, tumor-free mice did not show any tumor growth until 90 days, the latest time point observed.

Additionally, before and after rechallenge, we observed a substantial expansion of gp100 antigen reactive T cells in the blood of surviving mice (Fig. 5j). Furthermore, the retrieved Pmel T cells from the tumor-site maintained effector phenotype as evident from their reduced expression of FoxP3 (Fig. 5k), higher production of IFNγ, GzmB, (Fig. 5l), and enhanced expression of CXCR3 (Fig. 5m), in the case where the mice received Pmel-LC3-GFP^{pos} T cells. Corroborating this, Pmel-LC3-GFP^{pos} T cells showed an improved capacity to migrate in different lymphoid and non-lymphoid organs (Fig. S5f). Similarly, Pmel-LC3-GFP^{pos} T cells isolated from the spleen (Fig. S5g) and DLNs (Fig. S5h) display enhanced cytokine response after antigen rechallenge. Given the long-term tumor control observed with murine tumor cell line, we next determined if a similar strategy can control tumors in

Author Manuscript Author Manuscript Author Manuscript Author Manuscript

the human melanoma tumor model. To this end, h3T TCR transgenic mice (42) on C57BL6/LC3-GFP-RFP background were generated. Upon CO treatment h3T LC3-GFP^{pos} and LC3-GFP^{neg} T cells were FACS sorted before adoptively transferred into human melanoma 624-MEL bearing NSG mice. Like the murine tumor model, we observed LC3-GFP^{pos} T cells exhibited vastly improved tumor control than LC3-GFP^{neg} T cells in the human melanoma tumor model (Fig. S5i).

Since Sirt1 activator Resveratrol, mitochondrial fission inhibitor M1, and fusion activator Midvi stimulate mitochondrial function (5,43), we hypothesized that treating the LC3-GFP^{neg} T cells with these compounds could prevent the mitochondrial dysfunction and rescue the effector function in LC3-GFP^{neg} T cells. We noticed an increase in the GFP^{pos}RFP^{pos} and GFP^{pos} populations in LC3-GFP^{neg} T cells after Resveratrol and M1+Midvi treatment, suggesting an active autophagic process (Fig. S5j). Furthermore, both the compounds significantly increase the effector function (Fig. S5k) and ATP production in LC3^{-}GFP^{neg} T cells (Fig. S5l). These data suggest that rewiring the mitochondria in LC3^{-}GFP^{neg} T cells can rescue their effector function, and autophagy is required to rescue them from mitochondrial dysfunction.

T cells undergoing autophagy have distinct epigenetic and metabolic states.

A decline in mitochondrial quality control and turnover impairs the TCA cycle's function, leading to abnormal accumulation of metabolites (44,45). The accumulation of crucial metabolic intermediates, e.g., citrate (stimulates the production of acetyl-CoA in the cytosol), alpha-ketoglutarate (α-KG), succinate and fumarate, 2-hydroxyglutrate (2HG), regulates the activities of histone acetyltransferases (HATs), DNA demethylases (TET1-3) and histone demethylases (KDM2-7), the enzymes contributes to epigenetic programming and thus affect gene expression (44,45). So, the impaired mitochondrial respiratory function in LC3-GFP^{neg} T cell led us to examine the levels of key metabolites in LC3-GFP^{pos} and LC3-GFP^{neg} T cell subsets. The principal component analysis showed a distinct metabolic signature between these two subsets (Fig. 6a). Citrate, aspartate, and intermediates of pentose phosphate pathway and overall nucleotide pools were unchanged (Fig. 6b), consistent with the unaffected proliferation seen in the LC3-GFP^{neg} subset. However, we saw a diminished phosphoenolpyruvate level and significant glucose-6 phosphate and pyruvate level build-up in LC3-GFP^{neg} T cells (Fig. 6b). A significantly elevated level of amino acids, including Arginine, Tryptophan, Methionine, was also noted, indicating their impaired catabolism to downstream metabolites (Fig. 6b).

Moreover, LC3-GFP^{neg} T cells displayed a markedly higher 2HG, α-KG, succinate, and fumarate than LC3-GFP^{pos} T cells (Fig. 6b). Notably, the 2-HG/α-KG, succinate/α-KG, and fumarate/αKG ratios were significantly increased in LC3-GFP^{neg} T cells (Fig. 6c). Since 2-HG, succinate, and fumarate are potent inhibitors of histone demethylases and TETs(45), these results indicate the possibility of hypermethylation (of histone and DNA) in the LC3-GFP^{neg} subset. Furthermore, corroborating these ratios, we observed increased binding of 5-methylcytosine with the total genomic DNA in the LC3-GFP^{neg} subset (Fig. 6d), suggesting an elevated global DNA methylation. The concentration of intracellular α-KG is a metabolic regulator that governs the differentiation of Teff over Treg cells(46). So, we

Author Manuscript Author Manuscript Author Manuscript Author Manuscript

checked if treating the LC3-GFP^{neg} T cells with cell-permeable dimethyl-α-ketoglutarate (DM-αKG) to replenish the intracellular α-KG level can impact the DNA methylation and rescue the effector function in LC3-GFP^{neg} T cells. Treating LC3-GFP^{neg} T cells with DM-αKG decreased 5-methylcytosine binding with the total genomic DNA (Fig. 6d). In line with this, DM-αKG treatment increased the GFP^{pos}RFP^{pos} and GFP^{pos} populations (Fig. S6a). In addition, it restored the effector function in LC3-GFP^{neg} T cells (Fig. S6b), indicating its vital role in maintaining epigenetic profile and effector function in GFP^{pos} T cells.

Next, to determine if metabolite signaling cues remodel the epigenetic states of these two subsets that ultimately shape their effector function, we performed ATAC-seq (*a*ssay for *t*ransposase-*a*ccessible *c*hromatin using sequencing) on these subsets. For this purpose, Pmel-LC3-GFP-RFP T cells were activated, and CO was added at the last 24 hours of activation (when we obtained the highest percentage of LC3-GFP^{pos} T cells; (as in Fig. 5a), and then LC3-GFP^{pos} and LC3-GFP^{neg} T cells were FACS sorted. By examining chromatin accessibility with the ATAC-seq, we identified that 1029 genomic regions were characterized by higher chromatin accessibility in LC3-GFP^{pos} T cells, whereas 882 genomic regions had increased chromatin accessibility in LC3-GFP^{neg} T cells (Fig. 7a). LC3-GFP^{pos} T cells displayed significant enrichment of gene sets involved in persistent anti-tumor immunity (Notch signaling, longevity regulation, and HIF1 signaling pathway) (47,48) (Fig. S7a). Furthermore, LC3-GFP^{pos} CD8^{+} T cells contained open peaks for the long non-coding (lnc) RNA *Ifngas1* and *Ifnl2*, *Cmtr1*, *CD25h*, *Gzmm* (promotes interferon γ and Th1 response); *Sinhcaf*, *Hdac9*, *Hey1*, *Notch4* (Treg and TGFβ pathway regulatory genes); and *Bcl9l*, *Bcl9*, *Tcf4*, *Il7* (stemness trait regulator) (Fig. 7b). Whereas LC3-GFP^{neg} CD8^{+} T cells exhibited a different pattern with open peaks for *Foxp3*, *klrc1* (inhibitory marker); *Dnmt3a* is involved in the differentiation of exhausted CD8 T cells (Fig. 7b). This data led us to determine if similar differences in epigenetic states exist in LC3 GFP^{pos} and LC3 GFP^{neg} T cells after infiltrating the tumor *in vivo*. Thus, we compared the epigenetic signature of these subsets after isolating them from tumor sites (Fig. 7c). We observed that LC3-GFP^{pos} CD8^{+} TILs exhibits more accessible gene sets regulating pluripotency in stem cells, cytokine, and chemokine receptor signaling, whereas LC3-GFP^{neg} CD8^{+} TILs showed enriched gene sets coupled to inhibitory PI3/Akt axis (Fig. S7b) (49,50). In line with the *in vitro* epigenetic profiles, LC3-GFP^{neg} T cell showed more open TSS for *DNMT3L* (DNMT3L acts as a general stimulatory factor for *de novo* methylation by Dnmt3a) and *Dnmt3aos* (lncRNA regulates Dnmt3a expression leading to aberrant DNA methylation) (51,52) (Fig. 7d). Besides, they showed more open peaks for ERS responder ATF6 and PDIA5 (protein disulfide isomerase A5, necessary for ATF6α activation upon ERS(53) (Fig. 7d). Studies demonstrated that activation of ATF6 could promote apoptosis via upregulation of CHOP and engaging Xbp-1 and GP96 (54). Moreover, we overserved different immune regulatory molecules, including CD70 (limits T cell expansion *via* a regulatory T cell-independent mechanism that involves caspase-dependent T cell apoptosis and upregulation of inhibitory immune checkpoint) and IL27 (promotes the generation of IL-10-producing type 1 regulatory T (Tr1) cells that inhibit effector T cells molecules) have more open TSS in LC3-GFP^{neg} T cells isolated from tumor site (55,56) (Fig. 7d). In contrast, LC3-GFP^{pos} CD8 T cells maintained more open TSS for the genes like *IRF8*

Author Manuscript Author Manuscript Author Manuscript Author Manuscript

and *Pfn1* associated with T cell effector function (57) and survival (*stam*) (58) (Fig. 7d). Taken together, these results document distinct epigenetic states between LC3-GFP^{pos} and LC3-GFP^{neg} T cells. Sequencing read densities at a few selected genes of subset specific functional importance are shown in Fig. 7e (*in vitro*) and Fig. 7f (*in vivo*). In light of these observations, it will be interesting to dissect how signals from different metabolites modulate the epigenomes of LC3-GFP^{pos} and LC3-GFP^{neg} T cells and how this translates into modulation anti-tumor T-cell responses.

DISCUSSION

T cells within tumors exhibit a dynamic state with different epigenetic, transcriptional, and metabolic states resulting from chronic antigen stimulation or the immunosuppressive milieu (59,60). Previous studies have shown that TME progressively reprograms the T cells to a functionally exhausted state with impaired effector cytokines production and proliferation, loss of cytolytic ability, and enhanced expression of surface inhibitory receptors(60). In the past few years, several groups have demonstrated that sustained activation of ERS pathways in TME contributes to this path of dysfunctionality(9–12). Here we present experimental evidence indicating that transient (but not sustained) activation of ERS sensor PERK drives mitochondrial biogenesis and protective autophagy that builds a superior anti-tumor T cell, which can halt tumor growth upon ACT. Furthermore, the data revealed that T cells isolated from the tumor site could adapt to the transient ERS condition (imposed by CO) under a nutrient-rich environment. Furthermore, it facilitates the regaining of mitochondrial mass and effector function in TILs. Thus, this study highlights how the delicate balance of the ERS sensor activation (transient and heightened) regulates the switch between cellular outcomes (superior anti-tumor function and a dysfunctional state).

Earlier studies revealed that chronic antigen exposure leads to dysfunctional tumor-reactive T cells, and T cell functionality could be restored by increasing mitochondrial activity(2,4,6). Our results demonstrated that though both CO and TG treatment enhanced mitochondrial biogenesis and function at their sub-optimal doses (that does not cause cell death), TG-treated T cells showed increased IL10 production and slightly impaired effector cytokine production. This discrepancy might be explained by the sustained and increased *chop* level after TG treatment (until 48 hours), since the previous report has established a negative association between increased level of CHOP and effector cytokine production(11). On the contrary, owing to its short half-life CO upregulates CHOP expression for a short time and then declines after 6 hr. The data indicates that along with the magnitude, differences in the duration of the ERS stimuli tightly regulate the downstream signaling molecules and directly impact the cell fate decisions.

Our study showed that PERK is important in CO-mediated induction of mitochondrial biogenesis and protective autophagy *in vitro.* The CO treated mitochondria-rich, metabolically fit anti-tumor T cells show superior effector function in nutrient-deprived, hypoxic TME and thus exhibit efficient tumor control. On the contrary, some reports indicated that PERK ablated T cells are more efficient in controlling the tumor than WT T cells without prior ‘conditioning’ (12). ER stress response is mediated by three different sensor proteins, *viz*. IRE1a, PERK, and ATF6. However, they are not three linear and

Author Manuscript Author Manuscript Author Manuscript Author Manuscript

independent pathways. Instead, they are interconnected and work as a signaling network to efficiently handle stress conditions (61). Thus, along with PERK, IRE1 is also implicated in the activation of autophagy, and ATF6 activation plays a significant role in mitochondrial biogenesis (33). It has also been shown that ER luminal regions of PERK and IRE1α are structurally similar and even replaceable (61). Moreover, some studies reported that upon prolonged ER stress, IRE1α signaling is transient, whereas PERK signaling can be sustained. By contrast, in other experimental settings, IRE1α signaling can take over PERK signaling in response to prolonged stress, suggesting that these signaling branches are dynamic and, if needed, can compensate each other (61). So, we have to consider the involvement of other ER stress sensors in PERK KO cells and employ global approaches to comprehensively compare the two models (transient activation PERK vs. ablation of PERK signaling).

The physical interaction between ER and mitochondria coordinates ER–mitochondrial $Ca2^{+}$ and lipid transfer and regulates mitochondrial bioenergetics and apoptotic signaling (7). Mitochondrial-associated ER membranes are enriched with PERK, and genetic ablation of PERK disturbs ER–mitochondrial contacts (7). Corroborating with this, our finding showed that CO-exposed PERK-KO T cells exhibit defects in mitochondrial functions, whereas over-expression of PERK was detrimental and promoted apoptosis. In addition, the initial presence of PERK was found to be essential for shaping the CO-mediated T cell memory response since it was able to reduce translation due to Perk-mediated eIF2 phosphorylation. However, IL15 mediated reduced translation was independent of Perk and is likely dependent upon the Erk1/2 and pS6, as was shown recently (32). The inability of PERK-KO T cells to display CO-mediated memory T cell phenotype might highlight the role of PERK in ER mediated mitochondrial proteostasis and function(7). PERK is also substrate for the anti-oxidant protein Nrf2(7), and we have shown that anti-oxidant phenotype is a vital determinant of the Tcm cells (62).

The loss of mitochondrial mass has been shown to correlate with T cell dysfunctionality in TME (2). A recent study showed that T cells lacking mitochondria exhibit increased ROS coupled with exhaustion (4), and quenching ROS pharmacologically by L-NAC or overexpressing glutathione peroxidase 1 protected T cells from tumor-induced exhaustion. Our data suggest that CO treatment enhances mitochondrial mass and function. We examined if CO-treated T cells can retain their mitochondrial mass and functionality in the TME. We observed that T cells that underwent mitophagy exhibited an increased anti-oxidant capacity and “metabolically fit” phenotype that contributed to their potent anti-tumor phenotype upon ACT. Simultaneously, the T cells that failed to initiate the autophagic process showed high TGFβ signaling that increased their capacity to transdifferentiate to Treg’s and were thus unable to control tumor growth upon ACT. While nutrient starvation-induced autophagy is known to alter metabolite levels and T cell anti-tumor function (63), we demonstrate that PERK-dependent transient ER stress regulates mitophagy and the mitochondrial metabolites limit chromatin accessibility in T cells that contribute to potent anti-tumor phenotype and durable tumor control.

A recent study has shown that TILs have higher depolarized mitochondria due to reduced mitophagy and nicotinamide riboside (NR: a precursor for NAD^{+}) rescues TILs from

Author Manuscript Author Manuscript Author Manuscript Author Manuscript

terminal exhaustion (6) leading to improved tumor response. Using a dual reporter, LC3-GFP-RFP mouse, we show that in response to T cell receptor (TCR) engagement, a fraction of T cells and/or $CD8^+$ TILs upregulate LC3-GFP expression indicating that they are preparing to undergo autophagy. Exposing these TCR-activated T cells to transient ER stress (using CO) increases the LC3-GFP^{pos} population. We noted that the LC3-GFP^{pos} T cells inherit healthier mitochondria, and the composition of crucial Krebs cycle intermediates, e.g., citrate, α-KG, succinate, and fumarate, are different in LC3-GFP^{pos} and LC3-GFP^{neg} T cells. Our data established that distinct metabolite composition in LC3-GFP^{pos} and LC3-GFP^{neg} T cells correlates with altered DNA methylation content. This, in turn, shapes the epigenetic profile and gene expression of these two subsets. Importantly, we observed a more open TSS for DNA methyltransferase enzymes and molecules engaged in TGFβ signaling pathway in LC3-GFP^{neg} T cells, corroborating their immunosuppressive phenotype. This data opens the possibility of identifying a 'metabolically fit' T cell population based on 'early autophagy markers.' However, it warrants further study to establish autophagy as a marker of metabolically fit phenotype in T cell immunotherapeutic strategies.

Our data varies from the finding that loss of autophagy enhances $CD8^+$ T-cell mediated rejection of tumors (64). While this study showed that $Atg5^{-/-}$ $CD8^+$ T cells shift to a more glycolytic state, the OT-1 cells showed better tumor control than autophagy-sufficient T cells despite the effector memory phenotype. Contradictorily, we observed that $CD8^+$ T cells undergoing autophagy exhibit high mitochondrial dependence and Tscm phenotype supported by increased OCR. The difference is likely in evaluating the autophagy at the level of whole CD8 T cell subsets instead of delineating the CD8 fraction that has undergone autophagy versus those that have not (as done by us using the LC3-GFP RFP model). It is also possible that CO-induced mitophagy in melanoma epitope gp100 reactive T cells as opposed to "non-self" chicken ovalbumin reactive OT1-TCR could be the reason for notable differences. However, our data is similar to a recent publication where inducing autophagy has been shown to correlate with improved T cells persistence, stemness, and tumor clearance (63). Also, an earlier finding demonstrated that mitophagy is essential in maintaining NK cell functions, inhibiting the mTOR activity or activation of AMPK, resulting in increased autophagic activity and NK cell memory phenotype (38).

Overall, it is vital to understand the redundancies between the cellular organelle communicating with each other and how it maintains cellular function. While both ER and mitochondria are dysregulated in the tumor-infiltrating T cells (6,9), identifying a standard mechanism that facilitates the cross-talk between ER and mitochondria would help identify the targets that can be modulated to achieve robust tumor control. Our data suggest that transient stress that engages *Perk* could be an essential determinant in ER-mitochondrial inter-organelle signaling that shapes a strong anti-tumor T cell phenotype to improve immunotherapy.

Supplementary Material

Refer to Web version on PubMed Central for supplementary material.

Author Manuscript Author Manuscript Author Manuscript Author Manuscript

ACKNOWLEDGMENT:

The authors sincerely acknowledge help from Ms. Nancy Smythe for electron microscopy images at MUSC and Dr. Peng Gao at Northwestern Metabolomics Core. The work was supported in part by NIH grants P01CA098101 to JAD, R01GM130846 to VKG, and R21CA198646, R01CA236379, RO1CA250458, RO1DE030013, R41CA239952 to SM. DP was partly supported by NCN grant OPUS 2019/33/B/NZ5/03034. Support from Shared Instrumentation Grant S10OD018113 and Hollings Cancer Center Shared Resources (partly supported by P30 CA138313) at MUSC is also acknowledged.

REFERENCES

1. Crompton JG, Clever D, Vizcardo R, Rao M, Restifo NP. Reprogramming antitumor immunity. Trends Immunol 2014;35:178–85 [PubMed: 24661777]
2. Scharping NE, Menk AV, Moreci RS, Whetstone RD, Dadey RE, Watkins SC, et al. The Tumor Microenvironment Represses T Cell Mitochondrial Biogenesis to Drive Intratumoral T Cell Metabolic Insufficiency and Dysfunction. Immunity 2016;45:374–88 [PubMed: 27496732]
3. Sukumar M, Kishton RJ, Restifo NP. Metabolic reprograming of anti-tumor immunity. Curr Opin Immunol 2017;46:14–22 [PubMed: 28412583]
4. Scharping NE, Rivadeneira DB, Menk AV, Vignali PDA, Ford BR, Rittenhouse NL, et al. Mitochondrial stress induced by continuous stimulation under hypoxia rapidly drives T cell exhaustion. Nat Immunol 2021;22:205–15 [PubMed: 33398183]
5. Buck MD, O'Sullivan D, Klein Geltink RI, Curtis JD, Chang CH, Sanin DE, et al. Mitochondrial Dynamics Controls T Cell Fate through Metabolic Programming. Cell 2016;166:63–76 [PubMed: 27293185]
6. Yu YR, Imrichova H, Wang H, Chao T, Xiao Z, Gao M, et al. Disturbed mitochondrial dynamics in CD8(+) TILs reinforce T cell exhaustion. Nat Immunol 2020;21:1540–51 [PubMed: 33020660]
7. Rainbolt TK, Saunders JM, Wiseman RL. Stress-responsive regulation of mitochondria through the ER unfolded protein response. Trends Endocrinol Metab 2014;25:528–37 [PubMed: 25048297]
8. Bravo R, Vicencio JM, Parra V, Troncoso R, Munoz JP, Bui M, et al. Increased ER-mitochondrial coupling promotes mitochondrial respiration and bioenergetics during early phases of ER stress. J Cell Sci 2011;124:2143–52 [PubMed: 21628424]
9. Song M, Sandoval TA, Chae CS, Chopra S, Tan C, Rutkowski MR, et al. IRE1alpha-XBP1 controls T cell function in ovarian cancer by regulating mitochondrial activity. Nature 2018;562:423–8 [PubMed: 30305738]
10. Wu J, Chen YJ, Dobbs N, Sakai T, Liou J, Miner JJ, et al. STING-mediated disruption of calcium homeostasis chronically activates ER stress and primes T cell death. J Exp Med 2019;216:867–83 [PubMed: 30886058]
11. Cao Y, Trillo-Tinoco J, Sierra RA, Anadon C, Dai W, Mohamed E, et al. ER stress-induced mediator C/EBP homologous protein thwarts effector T cell activity in tumors through T-bet repression. Nat Commun 2019;10:1280 [PubMed: 30894532]
12. Hurst KE, Lawrence KA, Essman MT, Walton ZJ, Leddy LR, Thaxton JE. Endoplasmic Reticulum Stress Contributes to Mitochondrial Exhaustion of CD8(+) T Cells. Cancer Immunol Res 2019;7:476–86 [PubMed: 30659052]
13. Kamimura D, Bevan MJ. Endoplasmic reticulum stress regulator XBP-1 contributes to effector CD8+ T cell differentiation during acute infection. J Immunol 2008;181:5433–41 [PubMed: 18832700]
14. Li A, Song NJ, Riesenberg BP, Li Z. The Emerging Roles of Endoplasmic Reticulum Stress in Balancing Immunity and Tolerance in Health and Diseases: Mechanisms and Opportunities. Front Immunol 2019;10:3154 [PubMed: 32117210]
15. Wang Y, Zhang Y, Yi P, Dong W, Nalin AP, Zhang J, et al. The IL-15-AKT-XBP1s signaling pathway contributes to effector functions and survival in human NK cells. Nat Immunol 2019;20:10–7 [PubMed: 30538328]
16. Siracusa R, Schaufler A, Calabrese V, Fuller PM, Otterbein LE. Carbon Monoxide: from Poison to Clinical Trials. Trends Pharmacol Sci 2021;42:329–39 [PubMed: 33781582]

Author Manuscript Author Manuscript Author Manuscript Author Manuscript

17. Wang H, Gou W, Strange C, Wang J, Nietert PJ, Cloud C, et al. Islet Harvest in Carbon Monoxide-Saturated Medium for Chronic Pancreatitis Patients Undergoing Islet Autotransplantation. Cell Transplant 2019;28:25S–36S [PubMed: 31885286]
18. Almeida AS, Figueiredo-Pereira C, Vieira HL. Carbon monoxide and mitochondria-modulation of cell metabolism, redox response and cell death. Front Physiol 2015;6:33 [PubMed: 25709582]
19. Rhodes MA, Carraway MS, Piantadosi CA, Reynolds CM, Cherry AD, Wester TE, et al. Carbon monoxide, skeletal muscle oxidative stress, and mitochondrial biogenesis in humans. Am J Physiol Heart Circ Physiol 2009;297:H392–9 [PubMed: 19465554]
20. Corces MR, Trevino AE, Hamilton EG, Greenside PG, Sinnott-Armstrong NA, Vesuna S, et al. An improved ATAC-seq protocol reduces background and enables interrogation of frozen tissues. Nat Methods 2017;14:959–62 [PubMed: 28846090]
21. Zhang Y, Liu T, Meyer CA, Eeckhoute J, Johnson DS, Bernstein BE, et al. Model-based analysis of ChIP-Seq (MACS). Genome Biol 2008;9:R137 [PubMed: 18798982]
22. Long R, Salouage I, Berdeaux A, Motterlini R, Morin D. CORM-3, a water soluble CO-releasing molecule, uncouples mitochondrial respiration via interaction with the phosphate carrier. Biochim Biophys Acta 2014;1837:201–9 [PubMed: 24161358]
23. Oslowski CM, Urano F. Measuring ER stress and the unfolded protein response using mammalian tissue culture system. Methods Enzymol 2011;490:71–92 [PubMed: 21266244]
24. Larsson DE, Wickstrom M, Hassan S, Oberg K, Granberg D. The cytotoxic agents NSC-95397, brefeldin A, bortezomib and sanguinarine induce apoptosis in neuroendocrine tumors in vitro. Anticancer Res 2010;30:149–56 [PubMed: 20150630]
25. Hudson WH, Gensheimer J, Hashimoto M, Wieland A, Valanparambil RM, Li P, et al. Proliferating Transitory T Cells with an Effector-like Transcriptional Signature Emerge from PD-1(+) Stem-like CD8(+) T Cells during Chronic Infection. Immunity 2019;51:1043–58 e4 [PubMed: 31810882]
26. Guo Y, Xie YQ, Gao M, Zhao Y, Franco F, Wenes M, et al. Metabolic reprogramming of terminally exhausted CD8(+) T cells by IL-10 enhances anti-tumor immunity. Nat Immunol 2021;22:746–56 [PubMed: 34031618]
27. June CH, Riddell SR, Schumacher TN. Adoptive cellular therapy: a race to the finish line. Sci Transl Med 2015;7:280ps7
28. Rohaan MW, Wilgenhof S, Haanen J. Adoptive cellular therapies: the current landscape. Virchows Arch 2019;474:449–61 [PubMed: 30470934]
29. Cross BC, Bond PJ, Sadowski PG, Jha BK, Zak J, Goodman JM, et al. The molecular basis for selective inhibition of unconventional mRNA splicing by an IRE1-binding small molecule. Proc Natl Acad Sci U S A 2012;109:E869–78 [PubMed: 22315414]
30. McLaughlin M, Pedersen M, Roulstone V, Bergerhoff KF, Smith HG, Whittock H, et al. The PERK Inhibitor GSK2606414 Enhances Reovirus Infection in Head and Neck Squamous Cell Carcinoma via an ATF4-Dependent Mechanism. Mol Ther Oncolytics 2020;16:238–49 [PubMed: 32128359]
31. Araki K, Morita M, Bederman AG, Konieczny BT, Kissick HT, Sonenberg N, et al. Translation is actively regulated during the differentiation of CD8(+) effector T cells. Nat Immunol 2017;18:1046–57 [PubMed: 28714979]
32. Hurst KE, Lawrence KA, Robino RA, Ball LE, Chung D, Thaxton JE. Remodeling Translation Primes CD8(+) T-cell Antitumor Immunity. Cancer Immunol Res 2020;8:587–95 [PubMed: 32075802]
33. Senft D, Ronai ZA. UPR, autophagy, and mitochondria crosstalk underlies the ER stress response. Trends Biochem Sci 2015;40:141–8 [PubMed: 25656104]
34. Lee SJ, Ryter SW, Xu JF, Nakahira K, Kim HP, Choi AM, et al. Carbon monoxide activates autophagy via mitochondrial reactive oxygen species formation. Am J Respir Cell Mol Biol 2011;45:867–73 [PubMed: 21441382]
35. Joe Y, Kim S, Kim HJ, Park J, Chen Y, Park HJ, et al. FGF21 induced by carbon monoxide mediates metabolic homeostasis via the PERK/ATF4 pathway. FASEB J 2018;32:2630–43 [PubMed: 29295856]
36. Zheng M, Kim SK, Joe Y, Back SH, Cho HR, Kim HP, et al. Sensing endoplasmic reticulum stress by protein kinase RNA-like endoplasmic reticulum kinase promotes adaptive mitochondrial

Author Manuscript Author Manuscript Author Manuscript Author Manuscript

DNA biogenesis and cell survival via heme oxygenase-1/carbon monoxide activity. FASEB J 2012;26:2558–68 [PubMed: 22391129]

37. Puleston DJ, Zhang H, Powell TJ, Lipina E, Sims S, Panse I, et al. Autophagy is a critical regulator of memory CD8(+) T cell formation. Elife 2014;3
38. O'Sullivan TE, Johnson LR, Kang HH, Sun JC. BNIP3- and BNIP3L-Mediated Mitophagy Promotes the Generation of Natural Killer Cell Memory. Immunity 2015;43:331–42 [PubMed: 26253785]
39. Lin F, Wang ZV, Hill JA. Seeing is believing: dynamic changes in renal epithelial autophagy during injury and repair. Autophagy 2014;10:691–3 [PubMed: 24434795]
40. Wu YT, Tan HL, Shui G, Bauvy C, Huang Q, Wenk MR, et al. Dual role of 3-methyladenine in modulation of autophagy via different temporal patterns of inhibition on class I and III phosphoinositide 3-kinase. J Biol Chem 2010;285:10850–61 [PubMed: 20123989]
41. Field CS, Baixauli F, Kyle RL, Puleston DJ, Cameron AM, Sanin DE, et al. Mitochondrial Integrity Regulated by Lipid Metabolism Is a Cell-Intrinsic Checkpoint for Treg Suppressive Function. Cell Metab 2020;31:422–37 e5 [PubMed: 31883840]
42. Mehrotra S, Al-Khami AA, Klarquist J, Husain S, Naga O, Eby JM, et al. A coreceptor-independent transgenic human TCR mediates anti-tumor and anti-self immunity in mice. J Immunol 2012;189:1627–38 [PubMed: 22798675]
43. Peng K, Tao Y, Zhang J, Wang J, Ye F, Dan G, et al. Resveratrol Regulates Mitochondrial Biogenesis and Fission/Fusion to Attenuate Rotenone-Induced Neurotoxicity. Oxid Med Cell Longev 2016;2016:6705621 [PubMed: 26770656]
44. Martinez-Reyes I, Chandel NS. Mitochondrial TCA cycle metabolites control physiology and disease. Nat Commun 2020;11:102 [PubMed: 31900386]
45. Salminen A, Kauppinen A, Hiltunen M, Kaarniranta K. Krebs cycle intermediates regulate DNA and histone methylation: epigenetic impact on the aging process. Ageing Res Rev 2014;16:45–65 [PubMed: 24910305]
46. Klysz D, Tai X, Robert PA, Craveiro M, Cretenet G, Oburoglu L, et al. Glutamine-dependent alpha-ketoglutarate production regulates the balance between T helper 1 cell and regulatory T cell generation. Sci Signal 2015;8:ra97 [PubMed: 26420908]
47. Doedens AL, Phan AT, Stradner MH, Fujimoto JK, Nguyen JV, Yang E, et al. Hypoxia-inducible factors enhance the effector responses of CD8(+) T cells to persistent antigen. Nat Immunol 2013;14:1173–82 [PubMed: 24076634]
48. Kelliher MA, Roderick JE. NOTCH Signaling in T-Cell-Mediated Anti-Tumor Immunity and T-Cell-Based Immunotherapies. Front Immunol 2018;9:1718 [PubMed: 30967879]
49. van der Waart AB, van de Weem NM, Maas F, Kramer CS, Kester MG, Falkenburg JH, et al. Inhibition of Akt signaling promotes the generation of superior tumor-reactive T cells for adoptive immunotherapy. Blood 2014;124:3490–500 [PubMed: 25336630]
50. Klebanoff CA, Crompton JG, Leonardi AJ, Yamamoto TN, Chandran SS, Eil RL, et al. Inhibition of AKT signaling uncouples T cell differentiation from expansion for receptor-engineered adoptive immunotherapy. JCI Insight 2017;2
51. Chedin F, Lieber MR, Hsieh CL. The DNA methyltransferase-like protein DNMT3L stimulates de novo methylation by Dnmt3a. Proc Natl Acad Sci U S A 2002;99:16916–21 [PubMed: 12481029]
52. Li X, Zhang Y, Pei W, Zhang M, Yang H, Zhong M, et al. LncRNA Dnmt3aos regulates Dnmt3a expression leading to aberrant DNA methylation in macrophage polarization. FASEB J 2020;34:5077–91 [PubMed: 32052888]
53. Higa A, Taouji S, Lhomond S, Jensen D, Fernandez-Zapico ME, Simpson JC, et al. Endoplasmic reticulum stress-activated transcription factor ATF6alpha requires the disulfide isomerase PDIA5 to modulate chemoresistance. Mol Cell Biol 2014;34:1839–49 [PubMed: 24636989]
54. Kemp K, Poe C. Stressed: The Unfolded Protein Response in T Cell Development, Activation, and Function. Int J Mol Sci 2019;20
55. Iwasaki Y, Fujio K, Okamura T, Yamamoto K. Interleukin-27 in T cell immunity. Int J Mol Sci 2015;16:2851–63 [PubMed: 25633106]
56. Pot C, Apetoh L, Awasthi A, Kuchroo VK. Induction of regulatory Tr1 cells and inhibition of T(H)17 cells by IL-27. Semin Immunol 2011;23:438–45 [PubMed: 21893418]

Author Manuscript Author Manuscript Author Manuscript Author Manuscript

57. Miyagawa F, Zhang H, Terunuma A, Ozato K, Tagaya Y, Katz SI. Interferon regulatory factor 8 integrates T-cell receptor and cytokine-signaling pathways and drives effector differentiation of CD8 T cells. Proc Natl Acad Sci U S A 2012;109:12123–8 [PubMed: 22783014]
58. Yamada M, Ishii N, Asao H, Murata K, Kanazawa C, Sasaki H, et al. Signal-transducing adaptor molecules STAM1 and STAM2 are required for T-cell development and survival. Mol Cell Biol 2002;22:8648–58 [PubMed: 12446783]
59. Zhang X, Liu J, Cao X. Metabolic control of T-cell immunity via epigenetic mechanisms. Cell Mol Immunol 2018;15:203–5 [PubMed: 29082922]
60. Zebley CC, Gottschalk S, Youngblood B. Rewriting History: Epigenetic Reprogramming of CD8(+) T Cell Differentiation to Enhance Immunotherapy. Trends Immunol 2020;41:665–75 [PubMed: 32624330]
61. Hetz C The unfolded protein response: controlling cell fate decisions under ER stress and beyond. Nat Rev Mol Cell Biol 2012;13:89–102 [PubMed: 22251901]
62. Chakraborty P, Chatterjee S, Kesarwani P, Thyagarajan K, Iamsawat S, Dalheim A, et al. Thioredoxin-1 improves the immunometabolic phenotype of antitumor T cells. J Biol Chem 2019;294:9198–212 [PubMed: 30971427]
63. Vodnala SK, Eil R, Kishton RJ, Sukumar M, Yamamoto TN, Ha NH, et al. T cell stemness and dysfunction in tumors are triggered by a common mechanism. Science 2019;363
64. DeVorkin L, Pavey N, Carleton G, Comber A, Ho C, Lim J, et al. Autophagy Regulation of Metabolism Is Required for CD8(+) T Cell Anti-tumor Immunity. Cell Rep 2019;27:502–13 e5 [PubMed: 30970253]

Author Manuscript Author Manuscript Author Manuscript Author Manuscript

STATEMENT OF SIGNIFICANCE:

Transient activation of ER stress with carbon monoxide drives mitochondrial biogenesis and protective autophagy that elicits superior anti-tumor T cell function, revealing an approach to improving adoptive cell efficacy therapy.

Author Manuscript Author Manuscript Author Manuscript Author Manuscript

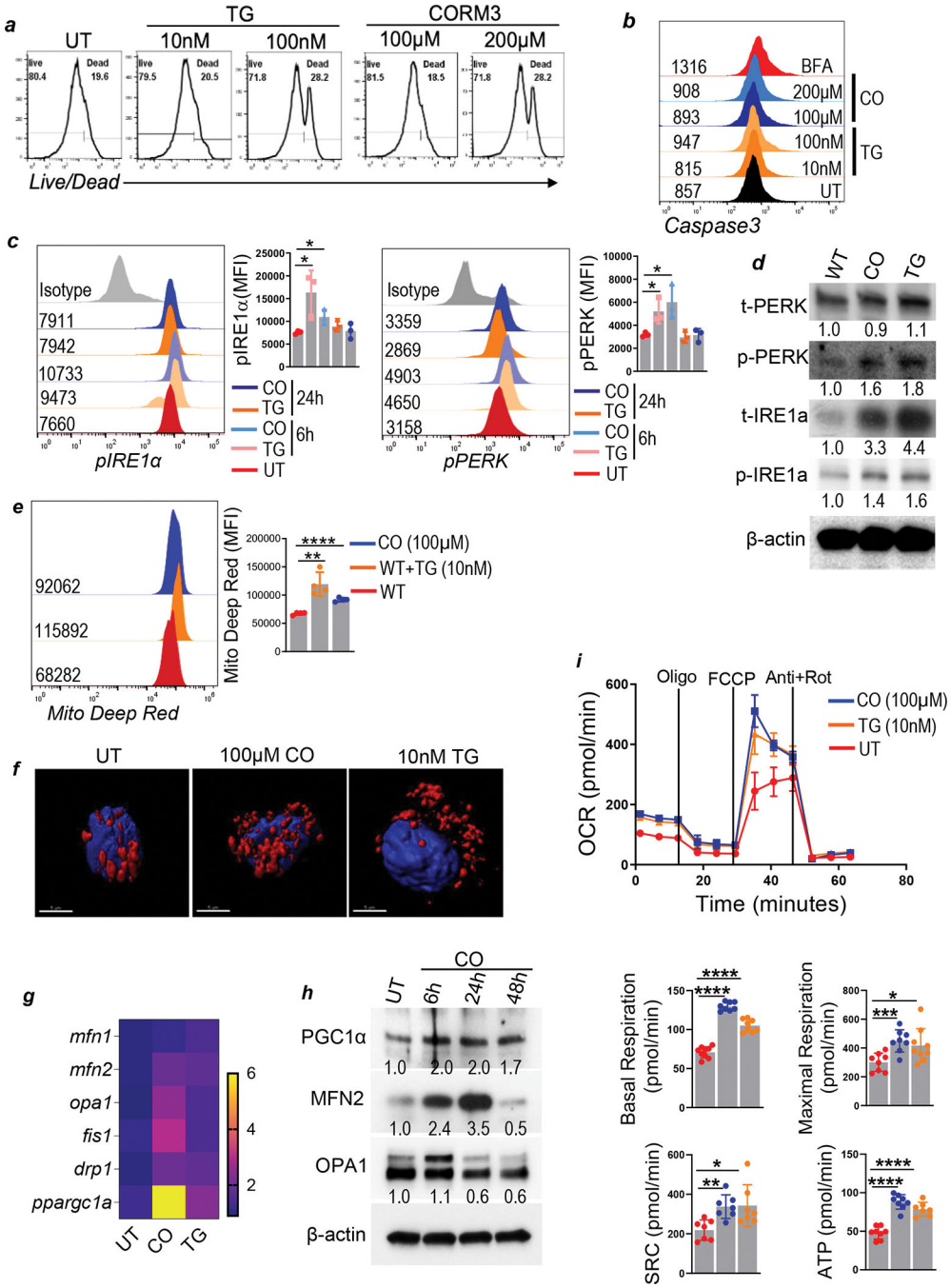

Figure 1: Moderate activation of the ERS sensor molecule enhances mitochondrial content and function in T cells.

(*a*) Pmel T cells were activated with gp100 for three days in IL2 (100 IU/ml). The indicated amount of Thapsigargin (TG) and CO were added to the culture media for 48 hours. Cell death was detected by flow cytometry using the LIVE/DEAD™ Fixable Yellow Dead Cell Stain Kit. **(*b*)** Cells from (*a*) were also used to determine Caspase 3 activity by flow cytometry using CaspGLOW™ Fluorescein Active Caspase-3 staining kit. Pmel T cells treated overnight with Brefeldin A (BFA: 2.5μM) were used as positive control. **(*c*)** Pmel T

Author Manuscript Author Manuscript Author Manuscript Author Manuscript

cells were activated with gp100 for three days in IL2 (100 IU/ml). CO (100 μM) and TG (10 nM) were added to the culture media for the last 6h and 24h (as indicated in the figure). Phosphorylation of IRE1α (*left panel*) and PERK (*right panel*) was determined by flow cytometry. The numerical values within the FACS overlay plots indicate mean fluorescence intensity (MFI). **(*d*)** Cells obtained from (*c*) were also used to perform western blot analysis. **(*e*)** Pmel T cells were activated with gp100 for three days in IL2 (100 IU/ml) for three days. Cells were left untreated or treated with either 10nM TG or with 100μM CO for the last 48 hours. The amount of active respiring mitochondria was determined using Mito Deep Red by flow cytometry. **(*f*)** Cells obtained from (*e*) were stained with Mito Red and DAPI, and confocal images were acquired to determine the location of mitochondria (in red) and nuclei (stained with DAPI; in blue). **(*g*)** Pmel T cells were activated with gp100 for three days in IL2 (100 IU/ml). Cells were left untreated or treated with 10nM TG or 100μM CO for the last 24 hours. mRNA was used to determine the expression of mitochondrial biogenesis-associated genes by qPCR. **(*h*)** Cells obtained from (*g*) were also used to perform western blot analysis. **(*i*)** Oxygen consumption rate (OCR) was determined under basal conditions and in response to indicated mitochondrial inhibitors in the cells obtained from (*e*). The graph on the upper panel represents the time course, and bar diagrams on lower panels represent basal oxygen consumption rate, maximal respiration, ATP production, and Spare respiratory capacity (SRC). N=3. *p-value* *<0.05, **<0.005, ***<0.0005.

Author Manuscript Author Manuscript Author Manuscript Author Manuscript

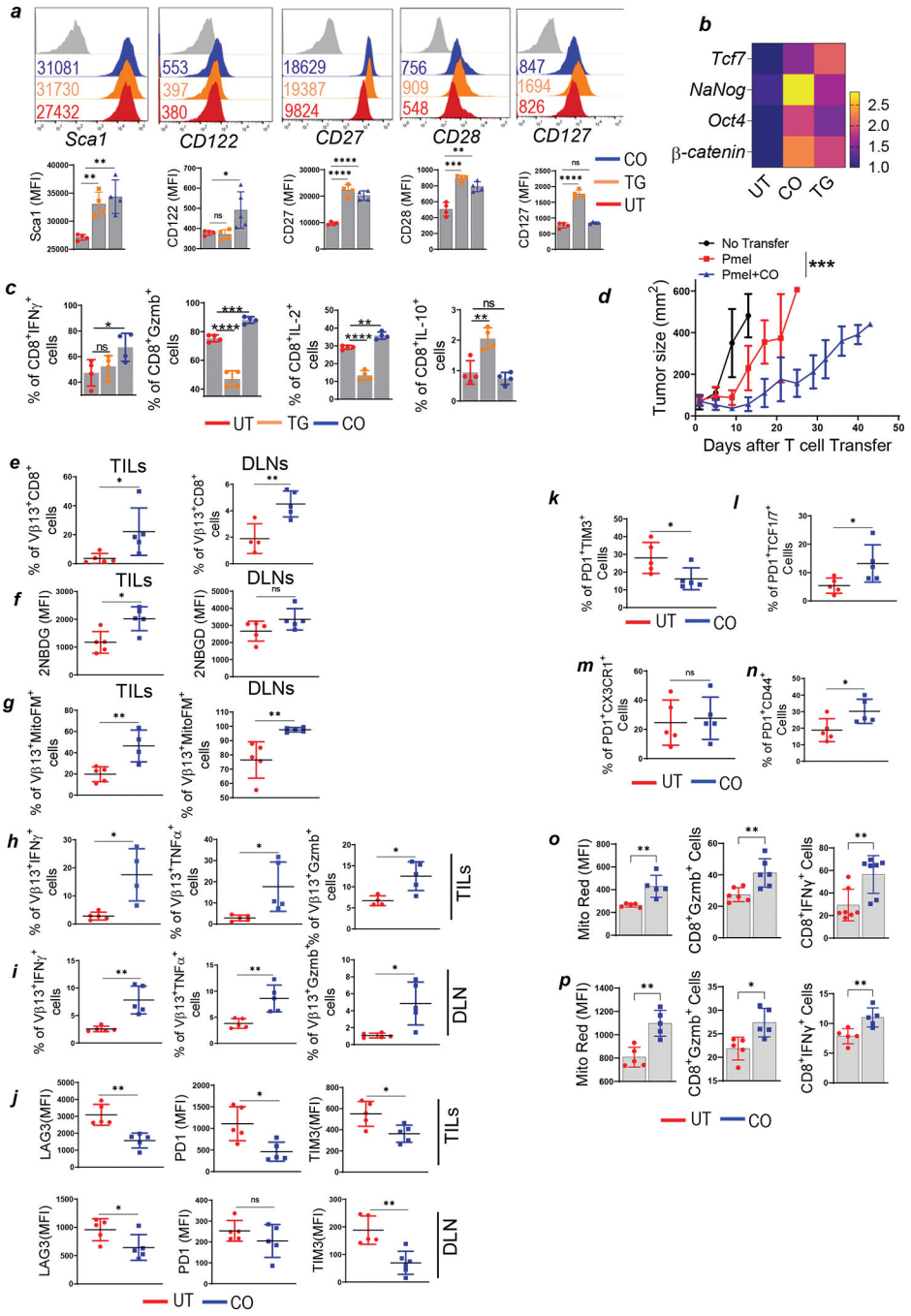

Figure 2: CO treatment improves T cell effector function and anti-tumor property in a preclinical model.

(*a*) Pmel T cells were activated with gp100 for three days in IL2 (100 IU/ml). Cells were left untreated or treated with either 10nM TG or with 100μM CO for the last 48 hours, after which fluorochrome-conjugated antibodies were used to determine the cell surface expression of stem cell antigen-1 (Sca1), CD122, CD27, CD28, and CD127. The numerical values within the FACS overlay plots indicate MFI. **(*b*)** The cells from (*a*) were used to determine the expression of stemness trait-associated genes by qPCR analysis. **(*c*)** The cells

Author Manuscript Author Manuscript Author Manuscript Author Manuscript

from (*a*) obtained after overnight restimulation with cognate antigen were used to determine intracellular cytokine (IFNγ, TNFα, IL10) and GzmB levels using flow cytometry. **(*d*)** C57BL/6 mice (n=15 mice/group) were inoculated subcutaneously (*s.c*) with 0.3×10^6 B16-F10 melanoma cells for 9 days, after which mice were either kept untreated as control or adoptively transferred with 1×10^6 Pmel or Pmel T cells cultured in the presence of CO (100μM; added in the culture media for last 48 hours). Tumor growth was measured using digital calipers twice weekly. A cumulative growth curve for each group is presented. **(*e*-*n*)** C57BL/6 mice (n=5 mice/group) were inoculated (*s.c*.) with 0.3×10^6 B16-F10 melanoma cells for 14 days, after which mice were adoptively transferred with 1×10^6 three days gp100 activated Pmel T cells or Pmel T cells treated with CO (100μM). After 12 days of T cells transfer, lymphocytes were retrieved from the excised tumor (TILs) and draining lymph nodes (DLN). The percentage of TCR transgenic T cell was determined by staining for Pmel TCR Vβ13 expression (*left panel*: TILs; *right panel*: DLNs). **(*f*)** Cells from (*e*) were analyzed by flow cytometry to determine 2NBDG uptake and **(*g*)** mitochondrial mass. **(*h, i*)** Retrieved lymphocytes from tumor and DLN were stimulated overnight with gp100 peptide antigen before staining with fluorochrome-conjugated antibodies to determine intracellular IFNγ, TNFα, and Gzmb levels**. (*j*)** Lag3, PD1, and TIM3 expression were also determined using flow cytometry. Data from multiple mice/groups is presented. Cells obtained from (*e)* were also evaluated for the expression of PD1 & TIM3 ***(k)*** PD1 & TCF1/7 ***(l)*** PD1 & Cx3cr1 ***(m)*** and PD1 & CD44 ***(n)*** together. *n*=5. *p-value* * <0.05, **<0.005. **(*o, p*)** Murine TILs and human lung cancer-derived TILs were used to determine mitochondrial mass using Mito Red (*left panels*). TILs were stimulated overnight with αCD3 and αCD28 antibodies (2ug/ml each) before staining with fluorochrome-conjugated antibodies to determine intracellular GzmB (*middle panel*) IFNγ (*right panel*) levels. n=5. *p<0.05, **p<0.005.

Author Manuscript Author Manuscript Author Manuscript Author Manuscript

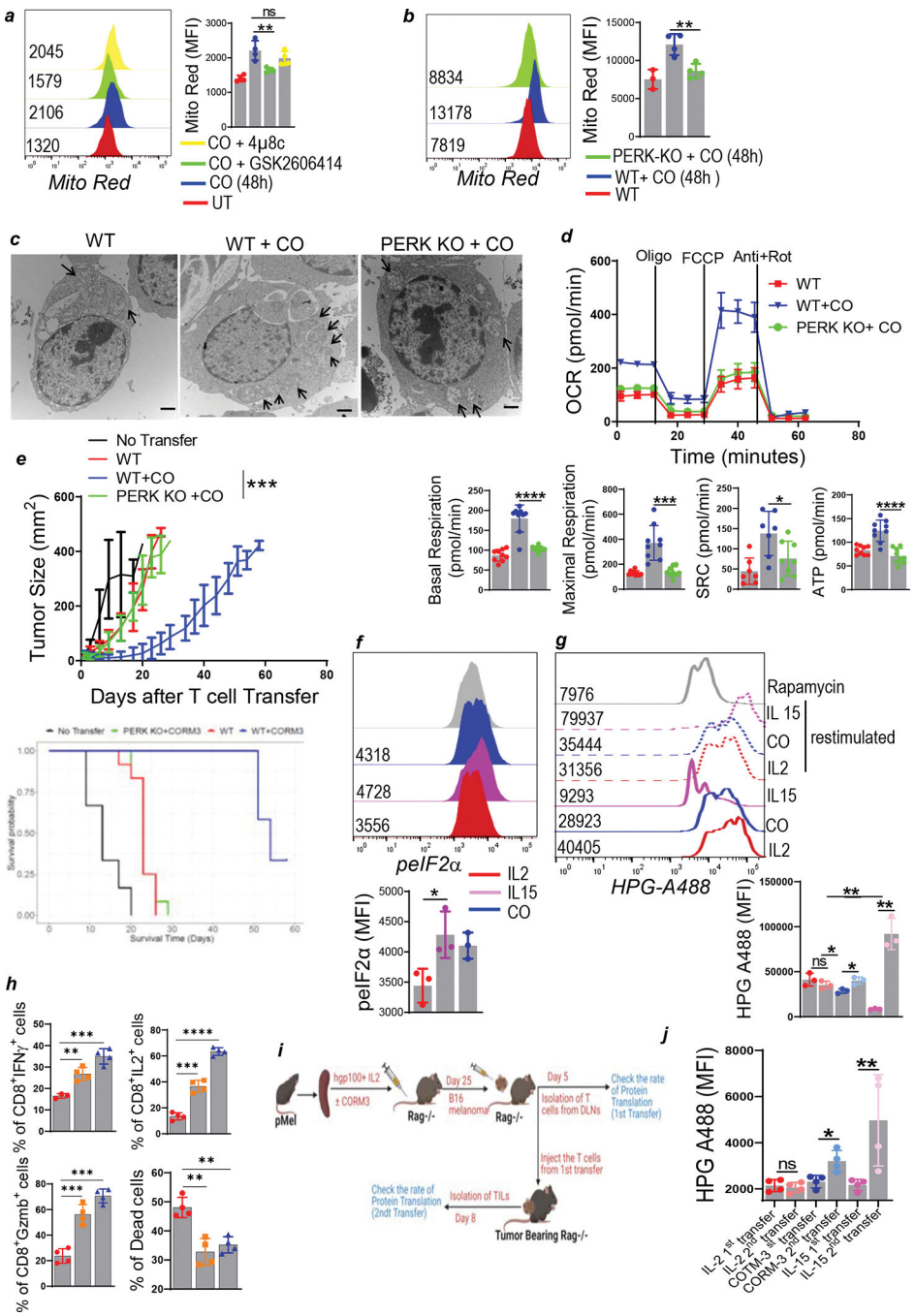

Figure 3: CO-mediated mitochondrial biogenesis is dependent on PERK activation.

(*a*) Pmel T cells were activated with gp100 for three days in IL2 (100 IU/ml). Some groups were pre-incubated for 1 hour with either 4μ8cGSK2606414 before CO (100μM) was added in the culture media for the last 48 hours. Mitochondrial mass was determined using Mito Red by flow cytometry. **(*b*)** Purified splenic T cells obtained from WT and PERK-KO mice were activated for three days. CO (100μM) was added to the culture media for the last 48 hours. Mitochondrial mass was determined by Mito Red using flow cytometry. Adjacent bar diagrams represent cumulative data from multiple repeat experiments. **(*c*)** Cells from (b)

Author Manuscript Author Manuscript Author Manuscript Author Manuscript

were also used for TEM analysis. **(*d*)** Real-time flux in OCR was measured using Seahorse in response to indicated mitochondrial inhibitors using the cells obtained from (b). The graph on the upper panel represents the time course, and bar diagrams on lower panels represent basal oxygen consumption rate, maximal respiration, ATP production, and Spare respiratory capacity (SRC). N=3. *p-value* *<0.05, **<0.005, ***<0.0005. **(*e*)** C57BL/6 HLA-A2+ mice (n=12 mice/group) with *s.c.* established 0.3×10^6 B16F10-$A2^+$ melanoma cells were adoptively transferred on day 9 with 1×10^6 WT or PERK-KO T cells retrovirally engineered to express melanoma epitope tyrosinase reactive TIL1383I TCR that was treated with CO (100μM) 48 hours. Tumor growth was measured using digital calipers twice weekly. The upper panels represent tumor growth curves, and the lower panel represents survival plots. **(*f*)** Pmel T cells were activated for 72 hours, and CORM-3 was added at the last 24h and 48h of activation. These differentially treated T cells were then tested for eIF2a phosphorylation by flow cytometry**. (*g*)**. Day 3 activated Pmel T cells were cultured for three more days, either in IL-2 (100 IU/mL) or IL15 (20ng/mL). CO was added at the last 48 hours in some IL-2 treated cells. Differentially treated Pmel T cells were then stimulated overnight with gp100 peptide antigen (0.001μg/ml) before enumerating the incorporation of L-homopropargylglycine (HPG) by flow cytometry. **(*h*)** Cells obtained from (g) were used to determine intracellular cytokine levels (IFNγ, GzmB, and IL2) production and cell death analysis using flow cytometry. The bar diagrams represent cumulative data from at least three repeat experiments. **(*i*)** Schematic diagram showing the strategy to check if CO pretreated and IL-2 or IL-15 treated Pmel T cells regain their protein translation activity in tumor-bearing mice after homeostatic proliferation in syngeneic host mice. Briefly, IL2, CORM-3 treated, or IL15 treated Pmel T cells were transferred into $Rag1^{-/-}$ mice. After 25 days, the recipient mice were injected with B16-F10 cells (1×10^4 cells/mouse). Five days later, CD8+ T cells were collected from DLNs. HPG incorporation was measured on a fraction of the retrieved cells, while the rest were transferred to a new set of tumor-bearing $Rag1^{-/-}$ hosts. After eight days, TILs were retrieved from tumors, and HPG incorporation was measured in $CD8^+$ TILs **(*j*)** The bar diagrams represent cumulative data from different mice (n=4). *p-value* *<0.05, **<0.005, ***<0.0005

Author Manuscript Author Manuscript Author Manuscript Author Manuscript

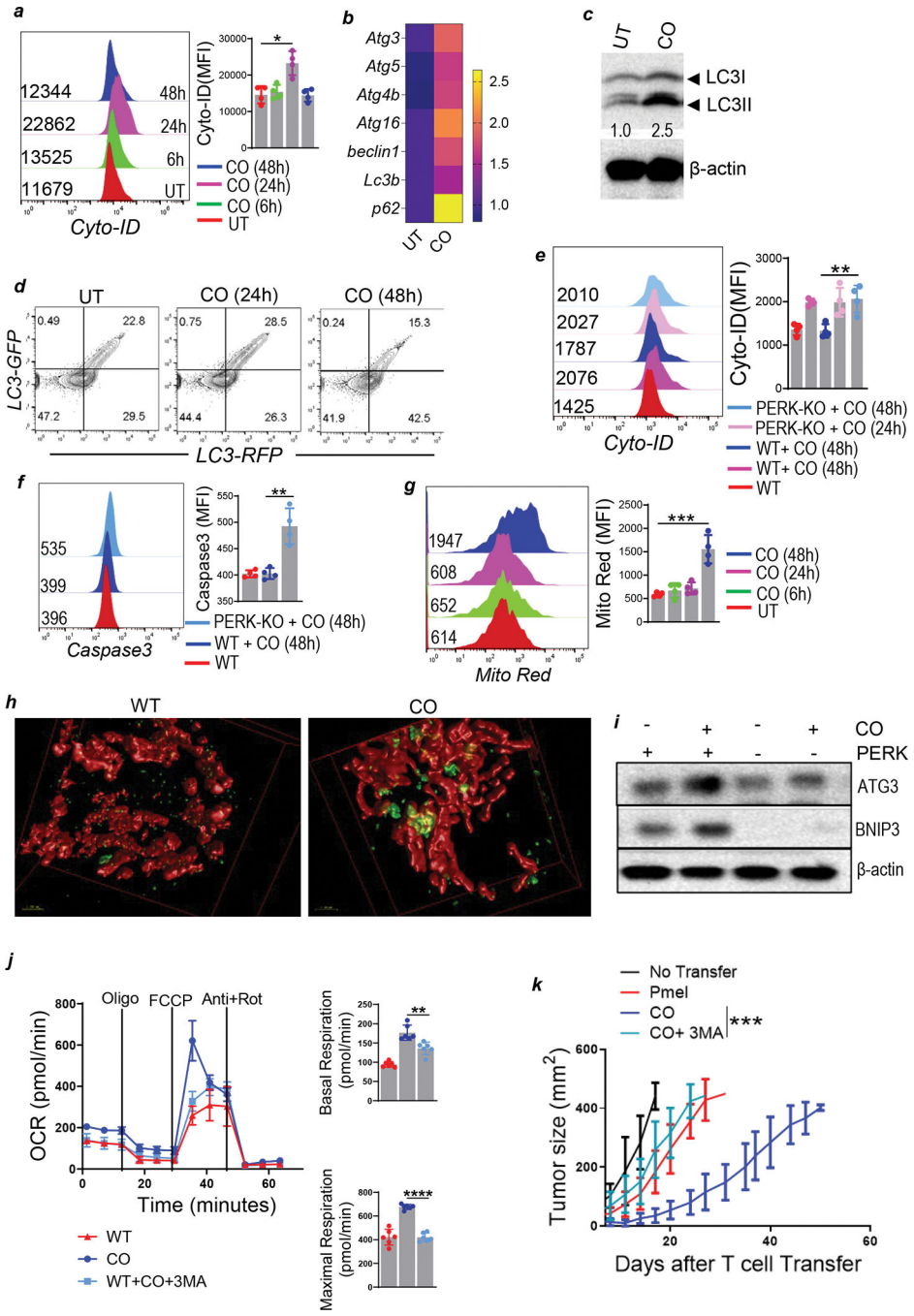

Figure 4: Transient PERK activation improves tumor control by engaging autophagy.

(*a*) Pmel T cells were activated with gp100 for three days in IL2 (100 IU/ml). CO (100μM) was added to the culture media for the last 6, 24, and 48 hours. The formation of autophagosome was analyzed using Cyto-ID dye by flow cytometry. The adjacent bar diagram represents the cumulative data from multiple experiments. **(*b*)** Untreated and 24h CO treated Pmel T cells obtained from (a) were used to determine the expression of different autophagy-associated genes by qPCR. **(*c*)** Cells described in Fig. 1c were also used to check lipidated the form of LC3I. The control β-actin blot is the same as shown in Fig. 1d.

Author Manuscript Author Manuscript Author Manuscript Author Manuscript

(*d*) Purified T cells obtained from Pmel-LC3-GFP-RFP mice were stimulated with αCD3 and αCD28 Ab for three days in IL2 (100 IU/ml). CO (100μM) was added to the culture media for the last 24 and 48 hours. The expression of GFP and RFP was analyzed by flow cytometry. **(*e*)** Purified splenic T cells obtained from WT and PERK-KO mice were activated for three days. CO (100μM) was added to the culture media for the last 24 and 48 hours. Cells were stained with Cyto-ID dye before being analyzed by FACS. **(*f*)** Purified splenic T cells obtained from WT and PERK KO mice were activated for three days. CO (100μM) was added to the culture media for the last 48 hours. Cells were used to determine Caspase 3 activity by flow cytometry. **(*g*)** Cells obtained from (a) were used to determine mitochondrial mass using Mito Red by flow cytometry. **(*h*)** Purified $CD8^+$ T cells obtained from Pmel /LC3-GFP-RFP mice were stimulated with αCD3 and αCD28 Ab for three days in IL2 (100 IU/ml). Cells were then transferred into gelatin-coated plates. CO (100μM) was added to the culture media, and after 24h, cells were stained with Mito Deep Red, fixed, and confocal images were taken. **(*i*)** Purified splenic T cells obtained from WT and PERK-KO mice were activated for three days. CO (100μM) was added to the culture media for the last 24 hours. Western blot analysis was performed to determine the level of indicated proteins. **(*j*)** Pmel T cells were activated with gp100 for three days in IL2 (100 IU/ml) for three days. In some wells, cells were pre-incubated for 1 hour with 3MA before the addition of CO. Cells were then used to determine real-time flux in OCR using Seahorse in response to indicated mitochondrial inhibitors. **(*k*)** C57BL/6 mice (n=15 mice/group) were inoculated (*s.c*) with 0.3×10^6 B16F10 melanoma cells for 9 days, after which mice were either kept untreated as control or adoptively transferred with 1×10^6 Pmel, Pmel T cells cultured in the presence of CO, or in the presence of CO and 3MA. Tumor growth was measured using digital calipers twice weekly. *p-value* *<0.05, **<0.005, ***<0.0005.

Author Manuscript Author Manuscript Author Manuscript Author Manuscript

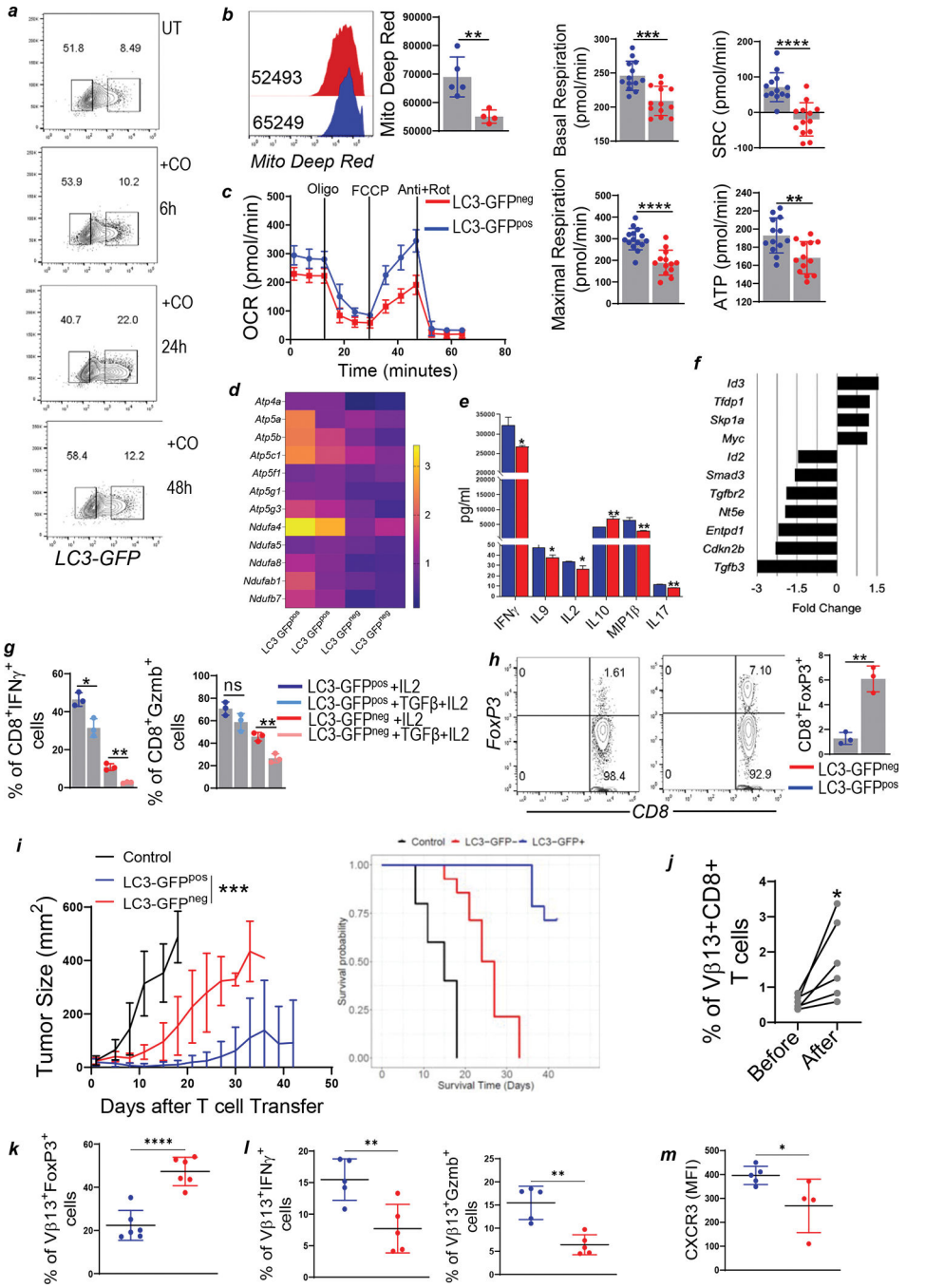

Figure 5: Cytoprotective autophagy contributes to healthy mitochondrial function and preserves vital anti-tumor effector function.

(*a*) Splenocytes obtained from Pmel /LC3-GFP-RFP mice were stimulated with αCD3 and αCD28 Ab for three days in IL2 (100 IU/ml). CO was added to the culture media for the last 6, 24, and 48 hours. The expression of GFP was analyzed by flow cytometry. **(*b*)** Splenocytes obtained from Pmel /LC3-GFP-RFP mice were stimulated with αCD3 and αCD28 Ab for three days in IL2 (100 IU/ml). LC3-GFP^{pos} and LC3-GFP^{neg} Cells were sorted after 24h CO treatment and stained with Mito Deep Red. **(*c*)** Real-time flux in OCR

Author Manuscript Author Manuscript Author Manuscript Author Manuscript

was measured using Seahorse in response to indicated mitochondrial inhibitors using the cells obtained from (b). **(*d*)** Cells obtained from (b) were also used to run mitochondria energy metabolism array. **(*e*)** Cells obtained from (b) were restimulated overnight with gp100 Ag, and multiplex ELISA was used for measuring cytokine secretion. **(*f*)** RNA obtained from (d) was used for RNA-seq analysis. **(*g*)** Cells obtained from (b) were further cultured for three days in the presence of TGFβ + IL2 and then restimulated overnight with cognate antigen. Intracellular production of IFNγ and GzmB was checked. **(*h*)** The expression of FoxP3 was determined using flow cytometry in the cells obtained from (b). Mean fluorescence intensity (MFI) for FoxP3 is plotted. **(*i*)** C57BL/6 mice (n=15 mice/group) subcutaneously injected with 0.3×10^6 B16F10 melanoma cells were treated on day 9 by adoptively transferring 0.3×10^6 Pmel LC3-GFP^{pos} or Pmel LC3-GFP^{neg} T cells. Untreated mice were kept as controls, and tumor growth was measured using digital calipers twice weekly. The upper panel represents tumor growth curves, and the lower panel represents the survival of different groups. *p-value* *<0.05, **<0.005, ***<0.0005. **(*j*)** The tumor-free mice that survived (i) were bled, and the abundance of the Vβ13$^+$CD8$^+$ population was checked at day 40. and the mice were then rechallenged with the same tumor. On day 5, they were bled again to check the frequency of Vβ13$^+$CD8$^+$ cells. **(*k*)** C57BL/6 mice (n=5 mice/group) were inoculated (*s.c.*) with 0.3×10^6 B16-F10 melanoma cells for 12 days, after which mice were adoptively transferred with 0.3×10^6 Pmel LC3-GFP^{pos} or Pmel LC3-GFP^{neg} T cells. After 15 days of T cells transfer, lymphocytes were retrieved from the excised tumor (TILs). The percentage of Vβ13$^+$FoxP3$^+$ T cell was determined by flow cytometry. **(*l*)** Cells obtained from (k) were stimulated overnight with gp100 peptide antigen before staining with fluorochrome-conjugated antibodies to determine intracellular IFNγ and GzmB levels. (***m*)** Cells obtained from (k) were used to analyze the percentage of Vβ13$^+$CXCR3$^+$ population by flow cytometry.

Author Manuscript
Author Manuscript
Author Manuscript
Author Manuscript

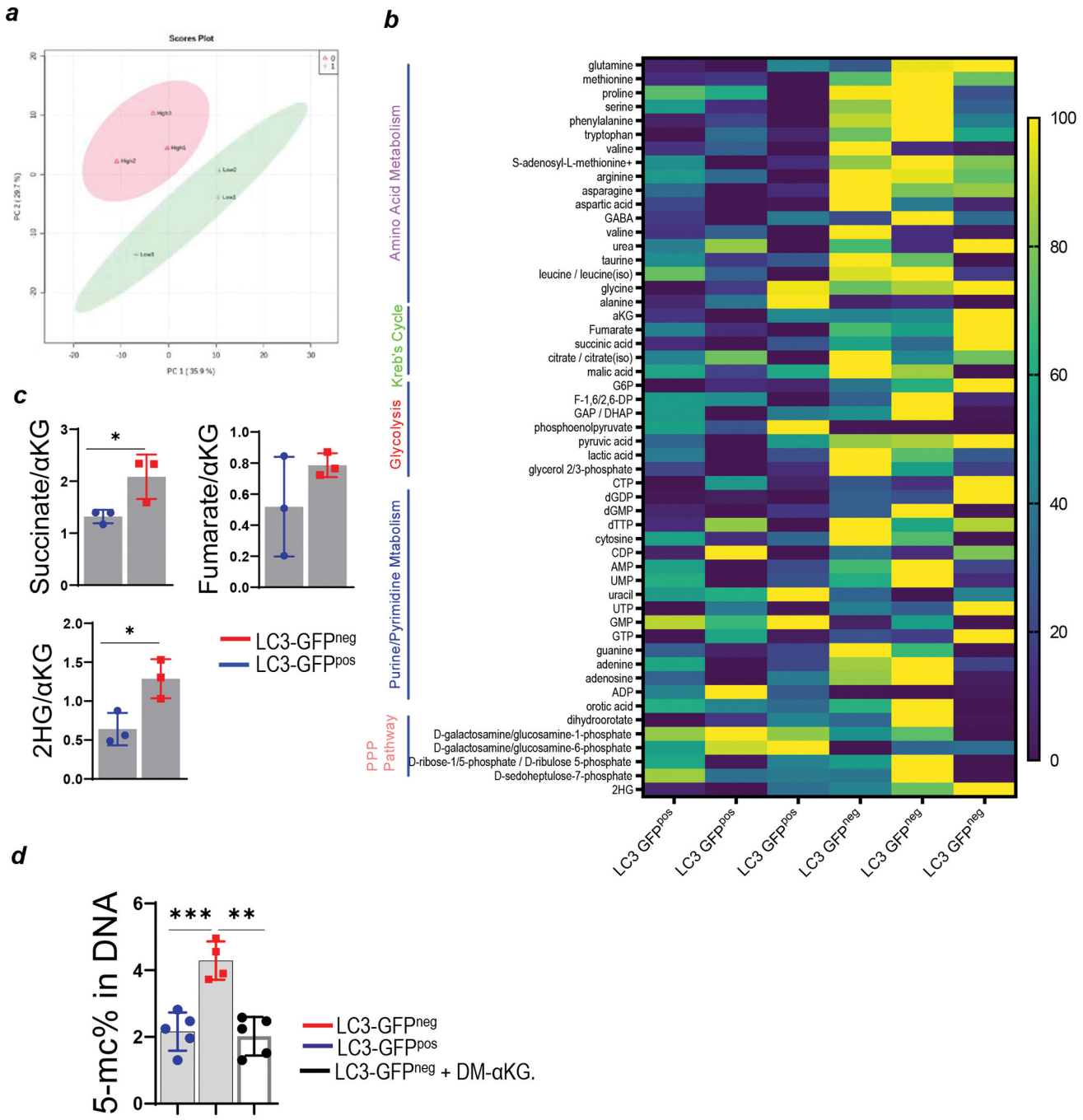

Figure 6: T cells undergoing autophagy have distinct metabolic states.

(a) Purified T cells obtained from Pmel /LC3-GFP-RFP mice were stimulated with αCD3 and αCD28 Ab for three days in IL2 (100 IU/ml). LC3-GFP^{pos} and LC3-GFP^{neg} Cells were sorted after 24h CO treatment and used for comprehensive metabolite analysis using mass spectrometry. The principal component analysis (PCA) is shown. ***(b)*** The heat map shows relative levels of metabolites in the cells obtained from (A). ***(c)*** The ratio of 2HG, succinate, and fumarate to αKG in LC3-GFP^{pos} and LC3-GFP^{neg} cells. ***(d)*** Purified T cells obtained from Pmel-LC3-GFP-RFP mice were stimulated with αCD3 and αCD28 Ab for three days

Author Manuscript Author Manuscript Author Manuscript Author Manuscript

in IL2 (100 IU/ml). Post 24h CO treatment, FACS sorted LC3-GFP^{pos} and LC3-GFP^{neg} cells were cultured in the presence or absence of dimethyl αKG (DMK) (3.5 mM) for two days. Total DNA was extracted from the differentially treated cells. The percentage of 5-methylcytosine was determined in 100 ng of DNA. N=3. *p-value* *<0.05, **<0.005.

Author Manuscript Author Manuscript Author Manuscript Author Manuscript

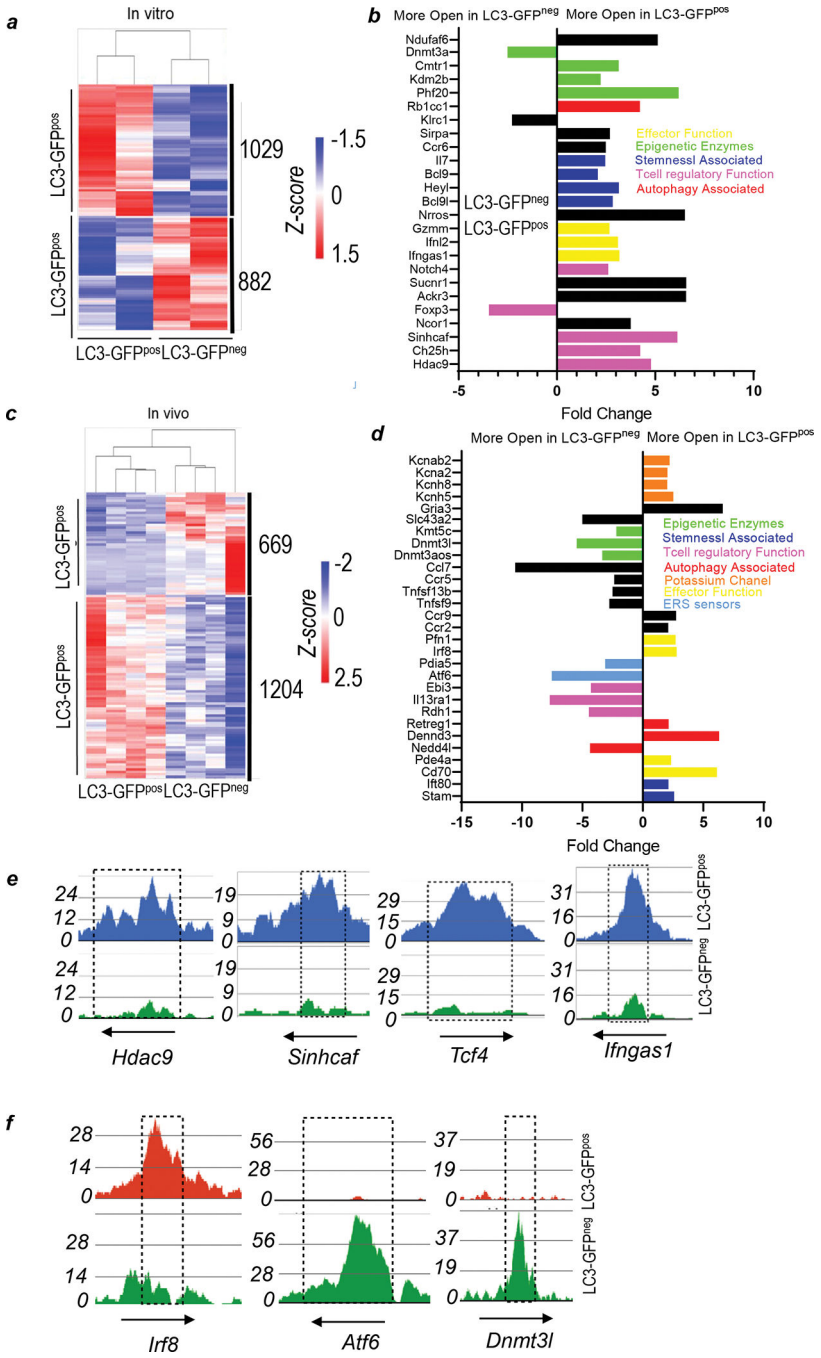

Figure 7: T cells undergoing autophagy have distinct epigenetic states.

(*a*) Purified T cells obtained from Pmel-LC3-GFP-RFP mice were stimulated with αCD3 and αCD28 Ab for three days in IL2 (100 IU/ml). LC3-GFP^{pos} and LC3-GFP^{neg} Cells were sorted after 24h CO treatment and used for ATAC-seq. A heat map with normalized chromatin accessibility exhibits cluster analysis of the differentially accessible peaks between LC3-GFP^{pos} and LC3-GFP^{neg} T Cells **(*b*)** The number of differentially open gene regulatory regions for genes of functional importance in LC3-GFP^{neg} (*left*) and LC3-GFP^{pos} (*right*). **(*c*)** C57BL/6 mice (n=4 mice/group) were inoculated (s.c) with 0.3×10^{6}

Author Manuscript Author Manuscript Author Manuscript Author Manuscript

B16-F10 melanoma cells for 12 days, after which mice were adoptively transferred with 0.3×10^6 Pmel LC3-GFP^{pos} or Pmel LC3-GFP^{neg} T cells. After 15 days of T cells transfer, lymphocytes were retrieved from the excised tumor (TILs). V$\beta13^+CD8^+$ population was sorted from the individual mouse by FACS and used for ATAC-seq. A heat map with normalized chromatin accessibility exhibits cluster analysis of the differentially accessible peaks between LC3-GFP^{pos} and LC3-GFP^{neg} T Cells. **(*d*)** The number of differentially open regulatory regions for genes of functional importance in LC3-GFP^{neg} (*left*) and LC3-GFP^{pos} (*right*). **(*e*, *f*)** Accessibility tracks for selected genes are significantly more open in (a) and (c), respectively.

Author Manuscript Author Manuscript Author Manuscript Author Manuscript

Table 1:

Key Resource Table.

REAGENT or RESOURCE	SOURCE	IDENTIFIER
Antibodies		
Anti-mouse CD3	BioXCell	Clone: 145-2C11; Cat# BE0001-1; RRID: AB_1107634
Anti-mouse CD28	BioXCell	Clone: 37.51; Cat# BE0015-1; RRID: AB_1107624
Anti-mouse IFNγ	BioXCell	Clone: XMG1.2; Cat# BE0055; RRID: AB_1107694
CD4-PE	eBioscience	Clone: GK5.1; Cat# 12-0041-83; RRID: AB_465506
FOXP3 -eFluor 660	eBioscience	Clone: FJK-16s; Cat# 50-5773-82
IRF-4-eFluor 660	eBioscience	Clone: 3E4; Cat# 50-9858-80; RRID: AB_2574393
CXCR3-PE	eBioscience	Clone: CXCR3-173; Cat# 12-1831-80; RRID: AB_1210734
CD4-PE/Cy7	Biolegend	Clone: GK5.1; Cat# 100422; RRID: AB_312707
CD4-APC	Biolegend	Clone: GK5.1; Cat# 100412; RRID: AB_312697
CD4-APC/Cy7	Biolegend	Clone: GK5.1; Cat# 100414; RRID: AB_312699
CD8-PE/Cy7	Biolegend	Clone: 53-6.7; Cat# 100722; RRID: AB_312761
CD8-APC	Biolegend	Clone: 53-6.7; Cat# 100712; RRID: AB_312751
CD8-FITC	Biolegend	Clone: 53-6.7; Cat# 100706; RRID: AB_312745
CD122 PerCP/Cyanine5.	Biolegend	Clone: TM-β1; Cat# 123212
Sca-1 APC/Cyanine7	Biolegend	Clone: D7; Cat# 108126
IFNγ-PE	Biolegend	Clone: XMG1.2; Cat# 505808; RRID: AB_315402
IFNγ-Alexa647	Biolegend	Clone: XMG1.2; Cat# 505814; RRID: AB_493314
CD28-PE	Biolegend	Clone: 37.51; Cat# 102106
CD27-APC	Biolegend	Clone: M-T271; Cat# 356409
CD62L-APC	Biolegend	Clone: MEL14; Cat# 104412; RRID AB_313099
CD44-PerCP/cye5.5	Biolegend	Clone: IM7; Cat# 103032; RRID AB_2076204
Gzmb-Alexa Fluor® 700	Biolegend	Clone: QA16A02; Cat# 372222
IL10-APC	Biolegend	Clone: JES5-16E3; Cat# 505010
IL2 -PE	Biolegend	Clone: JES6-5H4, Cat# 503808
PD-1-PE/Cyanine7	Biolegend	Clone:RMP1-30, Cat # 109110
LAG-3-PerCP/Cyanine5.5	Biolegend	Clone: C9B7W, Cat # 125212
Tim3-PE	Biolegend	Clone: RMT3-23, Cat # 119704
Vβ13-FITC	BD Biosciences	Clone: MR1 2–3; Cat# 553204; RRID: AB_394706
TNF alpha PE/Cyanine7	Biolegend	Clone: MP6-XT22; Cat# 506324
CD127-PE/Cyanine7	Biolegend	Clone: A7R34; Cat# 135014
Phospho-IREα (S724)	Thermo Fisher Scientific	Clone: Polyclonal; Catalog # PA1-16927
Mouse TGF-beta RII APC	R&D System	Clone: # Ile24Asp184 Accession # Q62312; Catalog# FAB532A-025
Anti-Goat Alexa647	Thermo Fisher Scientific	Clone: N/A; Cat# A21447; RRID: AB_141844
Phospho-PERK (Thr980)	Cell Signaling Technology	Clone: 16F8; Cat# 3179:

Author Manuscript Author Manuscript Author Manuscript Author Manuscript

REAGENT or RESOURCE	SOURCE	IDENTIFIER
Phospho-S6 Ribosomal Protein (Ser235/236)- Alexa647	Cell Signaling Technology	Clone: D57.2.2E; Cat# 4851; RRID: AB_916160
IRE1 α	Cell Signaling Technology	Clone: 14C10; Cat#3294
Anti-Rabbit HRP	Cell Signaling Technology	Clone: N/A; Cat# 7074S; RRID: N/A
Anti-Rabbit PE	Jackson ImmunoResearch Laboratories	Clone: N/A; Cat# 111-116-144; RRID: AB_2337985
Anti-Rabbit Alexa647	Jackson ImmunoResearch Laboratories	Clone: N/A; Cat# 111-607-003; RRID: AB_2338084
LC3A/B Ab	Cell Signaling Technology	Clone Rabbit polyclonal, Cat# 4108
Mitochondrial Dynamics Antibody Sampler Kit II	Cell Signaling Technology	Clone: N/A; Cat#74792
Perk Ab	Novus Biologicals	Clone: Rabbit polyclonal Cat# NBP1-78017
PGC1 α antibody	Millipore Sigma	Clone: Rabbit polyclonal Cat# AB3242
Chemicals, Peptides, and Recombinant Proteins		
4μ8c	Millipore Sigma	Cat# 14003-96-4
GSK2606414	Millipore Sigma	Cat# 1337531-89-1
3-Methyladenine	Millipore Sigma	Cat# 5142-23-4
CYTO-ID® Autophagy detection kit	Enzo	Cat# ENZ-51031-0050
MitoTracker® Red	Cell signaling technology	Cat# 9082
CaspGLOW™ Fluorescein Active Caspase-3 Staining	Thermo Fisher Scientific	Cat# 88-7004-42
LIVE/DEAD™ Fixable Yellow Dead Cell Stain Kit	Thermo Fisher Scientific	Cat# L34959
Click-iT™ HPG Alexa Fluor™ 488 Protein Synthesis Assay Kit	Thermo Fisher Scientific	Cat# C10428
MitoTracker™ Deep Red FM	Thermo Fisher Scientific	Cat# M22426
RetroNectin	Takara Bio	Cat# T202
2-Deoxy-D-glucose (2DG)	Sigma Aldrich	Cat# D6134
Antimycin A	Sigma Aldrich	Cat# A8674
Rotenone	Sigma Aldrich	Cat# R8875
Oligomycin	Sigma Aldrich	Cat# O4876
FCCP	Sigma Aldrich	Cat# C2920
IMDM	GE Healthcare, HyClone	Cat# SH30228.01
RPMI-1640 (methionine free)	Thermo Fisher Scientific	Cat# A1451701
Penicillin-Streptomycin	Corning	Cat# 30-001-CI
Fetal Bovine Serum (FBS)	Atlanta Biologicals	Cat# S11150
rTGFβ	Biolegend	Cat# 580702
rhIL2	NCI, Biological Resources Branch	https://ncifrederick.cancer.gov/research/brb/productDataSheets/cytokineHumanInterleukins/IL-2Bulk.aspx
Foxp3 / Transcription Factor Staining Buffer Set	Thermo Fisher Scientific	Cat# 00-5523
Fixation/Permeabilization Solution Kit	BD Biosciences	Cat# 554714
$hgp100_{25–33}$ peptide (KVPRNQDW)	Genscript	Cat# RP20344

Author Manuscript Author Manuscript Author Manuscript Author Manuscript

REAGENT or RESOURCE	SOURCE	IDENTIFIER
Nucleofector™ Kits for Mouse T Cells	Lonza	Cat# VPA-1006
RIPA Lysis Buffer	Thermo Fisher Scientific	Cat# 89900
NE-PER™ Nuclear and Cytoplasmic Extraction Reagents	Thermo Fisher Scientific	Cat# 78833
Critical Commercial Assays		
CellTrace™ Violet Cell Proliferation Kit	Thermo Fisher Scientific	Cat# C34557
MethylFlash Global DNA Methylation (5-mC) ELISA Easy Kit	Epigentek	Cat# P-1030-48
PPAR 96-Well Strip Plate	Cayman Chemical	Cat#10006887
Triglycerides Reagent	ThermoFisher Scientific	Cat# TR22421
Total Cholesterol Reagents	ThermoFisher Scientific	Cat# TR13421
Adenosine 5′-triphosphate (ATP) Bioluminescent Assay Kit	Abcam	Cat# ab113849
iScript™ cDNA Synthesis Kit	Biorad	Cat# 1708891
SsoAdvanced™ Universal SYBR® Green Supermix	Biorad	Cat# 1725274
Experimental Models: Cell Lines		
B16-F10	ATCC	CRL-6475
B16-F10-A2^{+}	Rolf Kiessling, Karolinska Institute, Stockholm, Sweden. *Mycoplasma* testing was done in Mehrotra lab.	N/A
Experimental Models: Organisms/Strains		
C57BL/6	Jackson Laboratory	Stock# 000664
C57BL/6-Tg(HLA-A2.1)1Enge/J	Jackson Laboratory	Stock# 003475
B6.129S7-*Rag1*^{tm1Mom}/J	Jackson Laboratory	Stock# 002216
CAG-RFP-EGFP-LC3 reporter mice	Jackson Laboratory	Stock# 027139
PERK$^{fl/fl}$ERT2^{cre} (tamoxifen-inducible)	Dr. Alan Diehl (Case Western University).	
Software and Algorithms		
FlowJo 10.2	TreeStar, OR	https://www.flowjo.com/solutions/flowjo/downloads/
Prism 8	GraphPad	https://www.graphpad.com/scientific-software/prism/
Agilent Seahorse Wave 2.4	Agilent	http://www.agilent.com/en-us/products/cell-analysis-(seahorse)/seahorse-wave-software
CFX Manager 3.1	Biorad	http://www.bio-rad.com/en-us/sku/soft-cfx-31-patch-cfx-manager-software-v3-1-upgrade

The table highlights the materials and resources that have been used to perform the experiments.